

**Cite this article:** Gervais P, Copland L, Medrzycka D, Noël B, Dahl-Jensen D, Alley KE (2025) Decades of supraglacial hydrological network evolution on Ellesmere Island's glaciers. *Journal of Glaciology* 71, e118, 1–23. <https://doi.org/10.1017/jog.2025.10095>

Received: 13 June 2025

Revised: 23 September 2025

Accepted: 24 September 2025

**Keywords:**

Arctic glaciology; climate change; glacier hydrology; glacier mapping; melt-surface

**Corresponding author:** Pénélope Gervais; Email: [pgerv058@uottawa.ca](mailto:pgerv058@uottawa.ca)

# Decades of supraglacial hydrological network evolution on Ellesmere Island's glaciers

Pénélope Gervais<sup>1</sup> , Luke Copland<sup>1</sup> , Dorota Medrzycka<sup>1</sup> , Brice Noël<sup>2</sup>, Dorthe Dahl-Jensen<sup>3</sup> and Karen E Alley<sup>3</sup> 

<sup>1</sup>Department of Geography, Environment and Geomatics, University of Ottawa, Ottawa, ON, Canada;

<sup>2</sup>Laboratory of Climatology, Department of Geography, SPHERES research unit, University of Liège, Liège, Belgium and <sup>3</sup>Centre for Earth Observation Science, Environment and Geography, University of Manitoba, Winnipeg, MB, Canada

## Abstract

Over the past two decades, the Canadian Arctic Archipelago has undergone significant glacier mass loss, driven primarily by surface melt. This study presents a detailed analysis of supraglacial drainage evolution along Ellesmere Island's ~830 km latitudinal extent using satellite imagery, historical aerial photographs and DEMs from 1959 to 2020. Analysis of five glaciers shows that drainage density ( $D_d$ ) has increased over time, driven by the expansion of perennial rivers, especially at higher elevations. Far northern glaciers exhibit stable, well-developed drainage systems, while southern glaciers show a relatively greater increase in canyon development since 1959. Cold surface ice in the north supports higher  $D_d$ , while southern glaciers with extensive sinks (moulins and large crevasses) exhibit stronger surface-to-bed connectivity. Despite increased channelization, sinuosity changes remain statistically insignificant, reflecting dynamic canyon behavior governed by surface slope and meltwater discharge. Results align with modeled increases in melt, especially on southern glaciers where supraglacial systems have expanded most rapidly. Continued equilibrium line altitude rise under future warming is expected to intensify melt and result in the expansion of supraglacial drainage systems up-glacier, particularly for glaciers with large amounts of ice at mid-elevation.

## 1. Introduction

The Arctic is undergoing rapid warming (Rantanen and others, 2022), which has been particularly pronounced in the Canadian Arctic Archipelago (Sharp and others, 2014). From 2000 to 2023, the Canadian Arctic Archipelago experienced the highest rate of glacier mass loss after Alaska, averaging  $53.6 \pm 4.7 \text{ Gt a}^{-1}$  (Zemp and others, 2025). Surface melt is the primary driver of this mass loss, accounting for 90% of the total mass losses in the northern Canadian Arctic Archipelago since 2005, leading to the formation and expansion of supraglacial hydrological networks (Millan and others, 2017; Lu and others, 2020). Supraglacial meltwater channels play a crucial role in a glacier's hydrological system by influencing surface mass balance (SMB) and routing meltwater that can eventually access englacial and subglacial pathways, thereby serving as an important connection between the surface and internal drainage systems (Pitcher and Smith, 2019). When supraglacial channels terminate in sinks such as moulins and large crevasses, large volumes of water can transfer to the glacier bed, impacting basal water pressure and the development of subglacial hydrological systems (Lu and others, 2020), in turn impacting ice motion (Schoof, 2010).

Advances in remote sensing (Yang and others, 2019; Bash and others, 2023), hydrological modeling (King and others, 2016) and field studies (St Germain and Moorman, 2019) have significantly enhanced our understanding of supraglacial hydrological networks. Despite these advances, supraglacial systems remain among the least studied hydrological components on Earth (Yang and others, 2019). Recent studies have begun to bridge this gap through the delineation of supraglacial hydrological features, which has been facilitated by the availability of high-resolution (e.g. WorldView-2 [WV2], 0.5 m; Yang and others, 2015a) to moderate-resolution (e.g. Sentinel-2, 10 m; Yang and others, 2017; Lu and others, 2020) satellite imagery and digital elevation models (DEMs) such as the ArcticDEM (Rippin and others, 2015; King and others, 2016; Yang and others, 2018; Bash and others, 2023). Recent studies in the Canadian Arctic Archipelago have contributed to the development or refinement of methodological frameworks for supraglacial hydrology mapping (Yang and others, 2019; Bash and others, 2023), assessed the evolution of the supraglacial drainage system over a single melt season (Lu and others, 2020), or have explored the relationship between surface melt and glacier dynamics for single points in time (Wyatt and Sharp, 2015; Yang and others, 2019). Despite these advances,

© The Author(s), 2025. Published by Cambridge University Press on behalf of International Glaciological Society. This is an Open Access article, distributed under the terms of the Creative Commons Attribution licence (<http://creativecommons.org/licenses/by/4.0/>), which permits unrestricted re-use, distribution and reproduction, provided the original article is properly cited.

research on supraglacial channels in the Canadian Arctic Archipelago remains limited, with most large-scale studies having taken place on the Greenland Ice Sheet (Yang and Smith, 2013; Yang and others, 2015a; King and others, 2016; Yang and others, 2017; Yang and others, 2019; Lu and others, 2020).

In the Canadian Arctic Archipelago, St Germain and Moorman (2019) made initial strides in addressing the gap in knowledge of supraglacial hydrological networks by studying the evolution of specific streams and rivers on Fountain Glacier, Bylot Island, although their research focused on a relatively short period (2010–17), capturing only a snapshot of their evolution. Although Kochtitzky and others (2023) mapped the development of supraglacial channels over the last ~60 years on Thores Glacier, northern Ellesmere Island, their study focused solely on major rivers in the ablation area and so did not capture fluctuations across the entire supraglacial system.

Recent findings from Greenland show that supraglacial drainage systems are highly dynamic, responding strongly to interannual variations in surface melt and the seasonal retreat of the snowline to higher elevations, which drives up-glacier expansion of drainage networks (Rawlins and others, 2023; Glen and others, 2025). Network morphology also evolves with time: changes in discharge influence channel incision and the transition from ephemeral surface streams to more deeply incised rivers and canyons. When combined with local glacier geometry, this will govern whether channels become perennial features or remain seasonally transient (St Germain and Moorman, 2019).

In this study, we examine how long-term climatic changes, particularly those influencing SMB and the position of the Equilibrium Line Altitude (ELA), have impacted the development of supraglacial hydrological features in the northern Canadian Arctic Archipelago. We aim to determine whether multi-decadal trends reveal up-glacier expansion of drainage networks and an increasing tendency for supraglacial channels to become perennial, rather than remaining primarily governed by annual variations in melt intensity. To address this, we employ a combination of optical satellite imagery, DEMs and historical aerial photographs to manually map supraglacial channel networks and assess their multi-decadal evolution across selected glaciers on Ellesmere Island in the northern Canadian Arctic Archipelago. We quantify their temporal changes over approximately 60 years by analyzing shifts in supraglacial drainage patterns and the composition of different channel types within the drainage system. We also evaluate spatial differences among glaciers to better understand the magnitude of change in supraglacial systems located in varied environmental settings. Together, these analyses provide a multi-decadal quantification of the supraglacial hydrological networks' evolution in this region, contributing novel insights into their response to climate warming.

## 2. Study area

Ellesmere Island (Umingmak Nuna), Nunavut (Fig. 1a), is the largest island in the northern Canadian Arctic Archipelago. Approximately 40% (~77 516 km<sup>2</sup>) of its area is covered by glaciers, of which ~53% are land-terminating and ~47% are marine-terminating (Millan and others, 2017; White and Copland, 2018). The island experiences a pronounced air temperature gradient from warmer mean annual temperatures in the south to colder temperatures in the north. There is also a precipitation gradient extending from southeast to northwest, with precipitation highest

along the coastlines facing Baffin Bay and decreasing with elevation and distance inland (Koerner, 1979).

The current study focuses on five glaciers (Fig. 1b–f), which were selected based on i) geographical distribution across the ~830 km latitudinal extent of Ellesmere Island, ii) data availability and iii) the presence of a perennial supraglacial drainage system (except for Sydkap Glacier, which was included for comparison). From north to south, these are:

1. Unnamed 1 Glacier (82.998°N, 72.855°W; Fig. 1b) is the smallest of the studied glaciers, with a basin area of approximately 18 km<sup>2</sup> and elevations ranging from ~30 to 980 m above sea level (a.s.l.). This glacier lies southeast of Ward Hunt Island near Canada's northernmost point and has never been studied.
2. Henrietta-Nesmith Glacier (81.857°N, 73.059°W; Fig. 1c), which drains the central eastern region of the Northern Ellesmere Icefield, covering ~1043 km<sup>2</sup> and with elevations ranging from ~100 to 2500 m a.s.l. Flowing from near the highest point on Ellesmere Island (Hattersley-Smith, 1961), it contributes substantially to Lake Hazen's hydrological input (Cavaco and others, 2019).
3. John Evans Glacier (79.650°N, 74.187°W; Fig. 1d) is a predominantly cold polythermal glacier, which covers an area of ~79 km<sup>2</sup> and has a length of about 15 km, with elevations ranging from ~100 to 1500 m a.s.l. Previous studies have documented a well-developed supraglacial drainage network below the ELA, which forms during a melt season lasting about 60 days (Bingham and others, 2006). The surface hydrological network is strongly linked to the subglacial drainage system (Bingham and others, 2005), with marked seasonal variability in glacier dynamics (Copland and others, 2003b; Bingham and others, 2006).
4. Unnamed 2 Glacier (78.793°N, 76.538°W; Fig. 1f) is a large land-terminating glacier that drains the northern part of the Prince of Wales Icefield, with a basin size of ~242 km<sup>2</sup> and an elevation range from ~30 to 1800 m a.s.l. Research conducted on nearby glaciers has reported rapid rates of mass loss since the mid-20th century (Bergsma and others, 1984), with rates nearly doubling between 1959–2001 and 2001–19, and the ELA rising by 77 m between 1974–82 and 2014–19 (Curley and others, 2021).
5. Sydkap Glacier (76.686°N, 85.461°W; Fig. 1e) is a large marine-terminating glacier with a basin area of ~475 km<sup>2</sup>, draining the southern side of Sydkap Ice Cap. It lost 36.41 km<sup>2</sup> of ice due to calving between 1959 and 2019 (Smith and others, 2020), resulting in a terminus retreat exceeding 9 km, one of the greatest in the Canadian Arctic Archipelago (Copland and others, 2003a).

## 3. Data and methods

### 3.1. Time-series analysis

Various recent optical satellite images (Sentinel-2, PlanetScope) were compared to ASTER and SPOT images, and historical aerial photographs, to document temporal and spatial changes in supraglacial hydrology across Ellesmere Island since the late 1950s (Tables A1 and A2, both in Appendix A). Two different kinds of analyses were undertaken, based on image quality and availability:

- a) Qualitative analysis: a series of images with approximately decadal separation was compiled for the five studied glaciers to qualitatively assess supraglacial drainage evolution, although

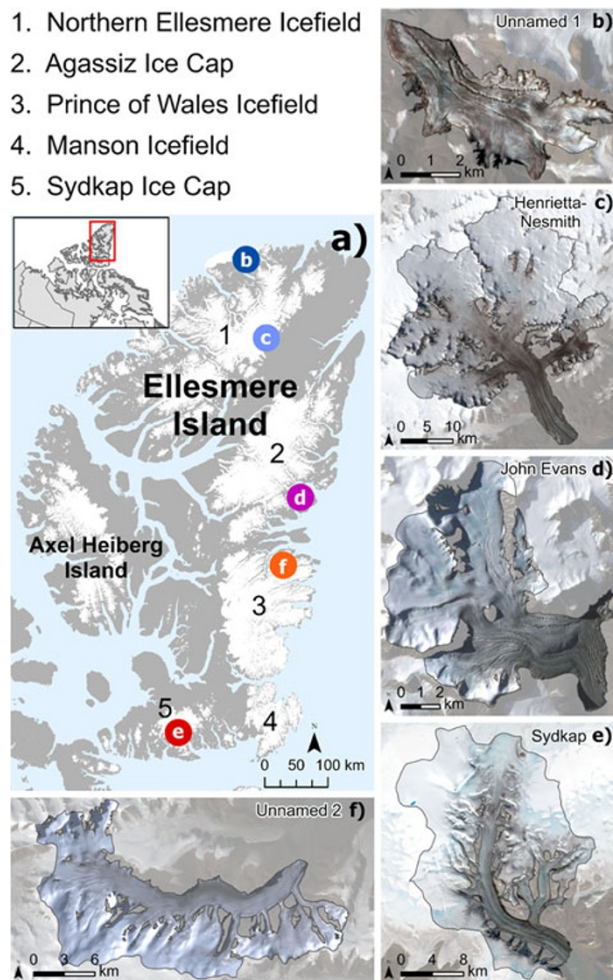


**Figure 1.** Location of the main icefields and ice caps, as well as the five studied glaciers, on Ellesmere Island. Projection: Canada Lambert Conformal Conic (main map), WGS UTM 16N (Sydkap Glacier) and WGS UTM 18N (other glaciers). Data: Panel (a)—Statistics Canada, 2016 Census—Provinces/territories—Cartographic Boundary File (statcan.gc.ca). Natural Resources Canada—Lakes, Rivers and Glaciers in Canada—CanVec Series—Hydrographic Features (Open Government Portal). Panels (b–f) —Glacier outlines are manually corrected Randolph Glacier Inventory v7 outlines. Satellite imagery: PlanetScope for panels (b, d, f) and Sentinel-2 for panels (c, e).

image availability, particularly before 2000, did not always allow for this. This included Sentinel-2, ASTER and SPOT imagery, with resolutions of  $\geq 10$  m, which could only resolve channels  $\sim 10$  m wide or larger. While unsuitable for precise quantification, these images provided valuable insights into the evolution of major channels.

b) Quantitative analysis: detailed mapping was conducted for 1959 and 2020 for the four northernmost glaciers. In 2020, supraglacial drainage networks were mapped in detail by manually delineating channels on 3 m-resolution PlanetScope images following specific criteria outlined in Section 3.6 (Table A2). Mapping for 1959 used  $\sim 0.6$  m-resolution historical aerial photographs (Table A1). To maintain consistency, only channels  $\geq 3$  m wide (five pixels in the air photos) were included, aligning with PlanetScope resolution. While images were examined at various scales to interpret features, all delineation was performed at scale of 1:2500 to ensure consistency across glaciers and years, as well as to enhance the differentiation of tones and textures (Bash and others, 2023). We note two important limitations in this mapping. First, full mapping was limited on Henrietta-Nesmith Glacier, due to poor aerial photograph image quality and snow cover in some images, particularly

those taken up-glacier. As a result, mapping focused on larger channels in the lower ablation area of this glacier. Second, quantitative analysis was not carried out on Sydkap Glacier because it does not exhibit a well-defined perennial drainage system.

For all analyses, cloud-free images were preferentially acquired in July and August, when snow cover was minimal, ensuring supraglacial drainage networks were fully developed and mapped under consistent surface conditions (Tables A1 and A2).

### 3.1.1. Equilibrium line altitude

The 2020 ELA was estimated from the average elevation of the snowline in cloud-free, late summer (July–August) Sentinel-2 and PlanetScope satellite imagery spanning 2016–20, using the methodology of Kochtitzky and others (2023; Table A2). Although this method does not account for the presence of superimposed ice that may exist below the ELA, Casey and Kelly (2010) found that the late-summer snowline offers the most reliable ELA estimate, showing strong agreement between remote sensing and in situ measurements. For each year, the snowline was manually delineated for all five glaciers by tracing the boundary between snow-covered and snow-free glacier surfaces in the late summer

imagery. Except for Unnamed 1, which only had images available in 2017 and 2020, the ELA on all other glaciers was traced on four to five images. Elevation values along each polyline were extracted from 2 m-resolution ArcticDEM strips from 2020, and an average ELA was calculated from these values (Table A3 in Appendix A). A contour line at the average elevation was subsequently drawn across each glacier surface to represent the ~2020 ELA. The standard deviation of the annual average snowline positions from 2016 to 2020 was used to represent the uncertainty in the ELA estimates, capturing interannual variability in late-summer snowline elevation.

The 1959 ELAs over the studied glaciers were estimated using regional reconstructions of the lowest ELAs in 1960, first conducted by Miller and others (1975) and later recreated by Wolken and others (2008). More recently, White and Copland (2018) digitized the recreated map of Wolken and others (2008) for northern Ellesmere Island and overlaid it on a Landsat 8 mosaic from 2015/16. This facilitated our estimate of the ELA for the smallest glacier, Unnamed 1, located near the northern coast of Ellesmere Island.

### 3.2. Historical aerial photographs

The earliest available imagery of the glaciers was 1959 panchromatic 1:60 000 scale vertical aerial photographs archived at the National Air Photo Library in Ottawa, Canada (Table A1). These images were acquired by the Royal Canadian Air Force and taken from an altitude of 9000 m a.s.l. using a Wild RC5A aerial film camera and Aviogon lens (15 AG). Images over sections of glaciers where channels were present were scanned at a resolution of 2033 dpi, resulting in a ground resolution of ~0.6 m. Lower-resolution photos scanned at 300 dpi with a ground resolution of ~4 m were used to provide coverage of the entire glacier surface for the quantitative analyses described later in the methods.

### 3.3. Satellite imagery

Satellite scenes used in both the qualitative and quantitative analyses were acquired from various sources (Table A2). SPOT 1–5 imagery covering the period from 1986 to 2015 was downloaded from the SPOT World Heritage data site (<https://regards.cnes.fr/user/swf/modules/60>). ASTER images, available since 1999 and acquired from the United States Geological Survey EarthExplorer database (<https://earthexplorer.usgs.gov/>), were used to fill gaps in the time series when SPOT images were not available. Sentinel-2 and PlanetScope imagery covered the most recent period since 2015, with Sentinel-2 images acquired from the Copernicus Open Access Hub (<https://www.copernicus.eu/en>) and the PlanetScope imagery downloaded through the Education and Research Program, courtesy of Planet Images (<https://www.planet.com/>). In addition, two WorldView-2 (WV2) and one WorldView-3 (WV3) image from 2022 covering the ablation area of Unnamed 2 and the entirety of Unnamed 1 glacier, respectively, were acquired through the European Space Agency's Third-Party Missions program and used as validation for the mapping of sinks.

### 3.4. Digital elevation models

To assist with mapping in shadowed and low contrast regions in satellite imagery, a shaded relief raster (hillshade model) was used as a support. Specifically, strips from the 2 m ArcticDEM version 4.1 from the Polar Geospatial Center (<https://www.pgc.umn.edu/data/arcticdem/>) were used for this purpose (Table A3).

The selected strips were closely aligned with the dates of the PlanetScope images for each glacier, ensuring consistency between datasets and reducing the risk of misclassifying channels with less well-defined banks (Bash and others, 2023).

The hillshade model was generated in the Quantum Geographic Information System (QGIS) v 3.24 utilizing the Hillshade tool within the GDAL library. To enhance the visibility of depressions, a solar altitude angle of 45° was chosen, and the lighting direction was aligned to be perpendicular to the predominant flow of the glacier, given that channels typically align parallel to the glacier flow (Bash and others, 2023). The hillshade model was produced without including shading from adjacent terrain, highlighting channel depressions with contrasting light and dark areas on either side (Bash and others, 2023).

### 3.5. Georeferencing

Manual georeferencing was performed in QGIS for each historical aerial photo, utilizing the 2020 PlanetScope scenes of each glacier as the master imagery. Apart from Unnamed 1 Glacier, which was fully covered by a single photo, all other glaciers required two to six photos to cover their entire surface. In such cases, the aerial photo that captured the glacier's terminus was initially georeferenced to its corresponding 2020 PlanetScope image. Subsequently, overlapping sections of the other aerial photos from that glacier were aligned to the previously georeferenced photo, while non-overlapping sections were directly aligned to the Planet imagery, ensuring improved alignment at the boundary of overlapping photos. Processing statistics of the final georeferenced products are provided in Table 1; the mean error reflects the average deviation between actual ground control point positions and their positions predicted by the transformation.

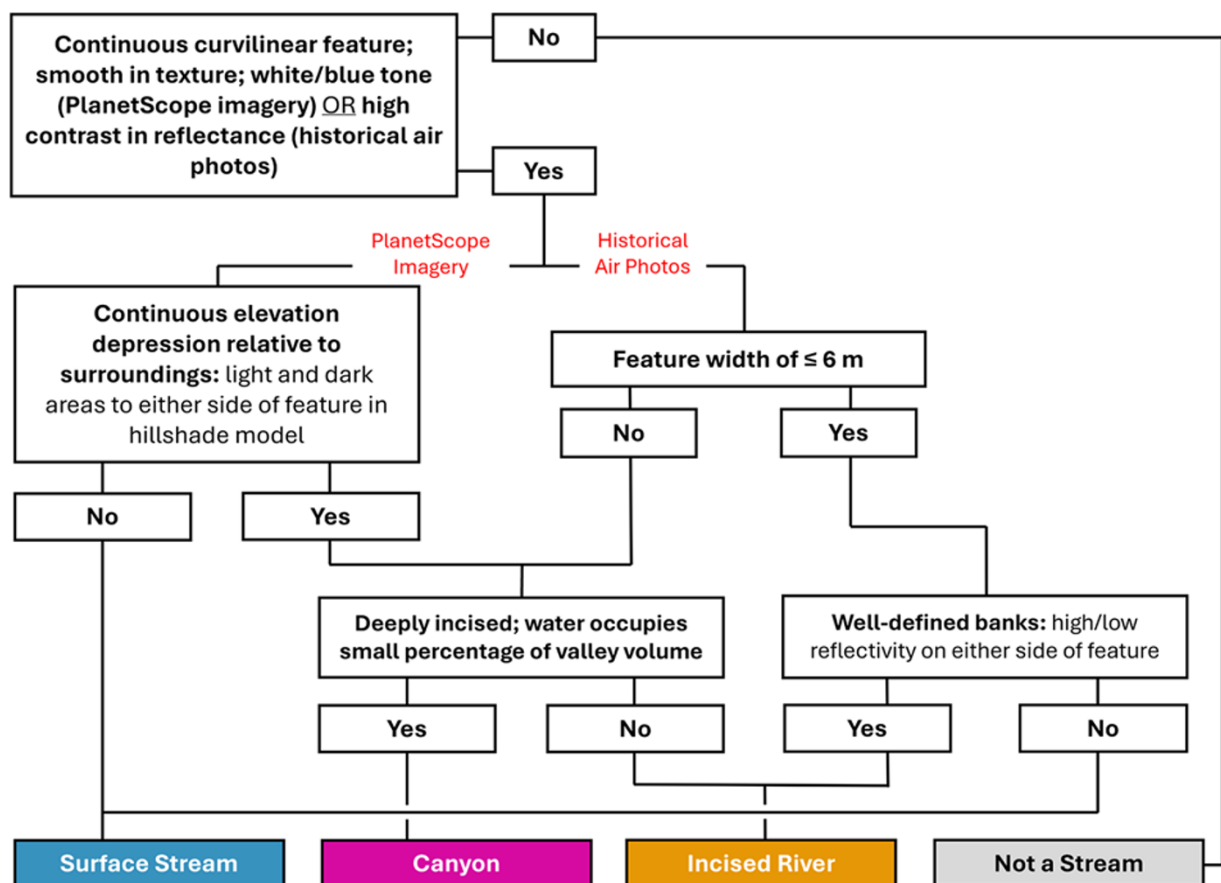
### 3.6. Channel mapping criteria

Although various automated and semi-automated methods have been developed to map supraglacial features, such as using spectral indices to detect water (Yang and Smith, 2013; Lu and others, 2020; Bash and others, 2023) or DEM-based hydrological modeling (Rippin and others, 2015; King and others, 2016; Yang and others, 2019) to infer flow paths, their application to long-term studies remains challenging due to the scarcity of high-quality data and inconsistencies in the spatial and spectral resolution between contemporary and historical imagery. Consequently, we manually identified and delineated supraglacial channels in this study. While manual mapping introduces potential uncertainty due to user bias, subjectivity was minimized by applying a consistent set of morphological and textural criteria (described below) and by having all delineations performed by a single analyst.

Following the terminology of Bash and others (2023), channels were identified based on their curvilinear shape, smooth texture and distinct blue/white tones in multispectral PlanetScope imagery. A curvilinear shape, with smooth, sinuous outlines and few sharp angles, distinguishes natural water channels from features like crevasses. Channels also exhibited a homogeneous reflectance pattern, appearing smooth in texture in the multispectral imagery. While maintaining the same morphology, Lampkin and VanderBerg (2014) also note that supraglacial channels show high contrast against the surrounding ice in panchromatic imagery (historical air photos), appearing darker. In this study, high mapping confidence was ensured by only including continuous channels, excluding features with repetitive breaks.

**Table 1.** Georeferencing statistics for historical aerial photographs

Glacier	Image ID	Total GCPs	Transformation	Residual pixel range	Mean Error (m)
Unnamed 2	A16613_106	17	Polynomial 3	1.13–23.59	18.61
Unnamed 2	A16726_084	15	Polynomial 3	0.11–17.25	13.36
Unnamed 2	A16679_073	17	Polynomial 3	1.64–22.41	23.05
Unnamed 2	A16974_023	18	Polynomial 3	3.90–18.53	19.36
Unnamed 2	A16974_025	11	Polynomial 1	1.12–36.42	24.86
Unnamed 2	A16679_072	14	Polynomial 1	3.13–33.89	20.04
John Evans	A16607_193	12	Polynomial 3	0.07–11.21	12.23
John Evans	A16607_192	20	Polynomial 3	1.80–14.86	10.20
John Evans	A16616_059	14	Polynomial 3	1.81–16.24	16.86
Henrietta-N	A16613_035	14	Polynomial 3	0.30–9.79	9.05
Henrietta-N	A16679_155	22	Polynomial 3	2.93–28.46	23.75
Henrietta-N	A16687_069	18	Polynomial 3	1.50–12.89	10.00
Unnamed 1	A16708_005	11	Polynomial 3	0.067–6.43	8.66

**Figure 2.** Decision tree for classifying supraglacial channels in imagery. Sections of the channel network are examined, and channels are classified as surface streams, incised rivers or canyons.

Once mapped, channels were classified according to terminology developed by St Germain and Moorman (2019), categorizing supraglacial channels into three main classes: surface, incised and canyons. Surface streams were identified by a valley depth-to-width ratio of less than one, meaning they lacked a distinct depression in the 2 m ArcticDEM but remained visible in PlanetScope imagery (Fig. 2 and Fig. A1 in Appendix A). Since no hillshade model was available for 1959, surface streams in historical aerial photographs were identified using image interpretation techniques (Bash and others, 2023) and relied on the concept that channel width and depth are positively correlated (St Germain and Moorman, 2019). The threshold beyond which depressions were

no longer discernible in the 2020 hillshade model (~6 m or two pixels in PlanetScope imagery) was used as a reference. Channels of this width in the 1959 aerial photographs, lacking clearly defined banks, were classified as surface streams. Well-defined channel banks suggest an incised feature where the valley depth-to-width ratio would likely be more than one, indicating that the channel is not of surface nature.

In contrast to surface streams, canyons are readily discernible in both satellite imagery and aerial photographs due to their substantial size and perennial presence. These deep, well-defined channels typically contain flowing water that occupies only a small portion of their valley volume (Fig. 2 and Fig. A1). Their prominent

banks, often casting shadows, further distinguish them in satellite imagery.

All remaining channels, those deeper than surface streams but smaller than canyons, were classified as incised rivers. These channels exhibited strong contrast on either side due to well-defined banks and appeared as continuous features in the hillshade model. The complete mapping workflow is summarized in Fig. 2, and examples of each channel class, as they appear in the imagery and hillshade models, are provided in Fig. A1 (Appendix A).

### 3.6.1. Uncertainty quantification

To quantify uncertainty in channel length measurements, we assumed a positional error of  $\pm 1$  pixel at both the start and endpoints of each digitized channel. When a channel flowed into another channel, its endpoint was excluded from the calculation to avoid double-counting. The cumulative uncertainty for each glacier was then estimated by multiplying the total number of considered start and endpoints by the pixel size. This approach was also applied to estimate the uncertainty in the total length of the individual channel classes.

### 3.7. Hydrography quantification

Several components of hydrography were derived from the final channel polylines, including total channel length, proportions of total length (PTL), drainage density ( $D_d$ ) and sinuosity.

$D_d$  standardizes channel length by glacier area, making it useful for comparing supraglacial networks across glaciers with varying surface areas and assessing channel abundance at different elevations. Here,  $D_d$  was calculated as the total channel length (km) divided by the glacier surface area ( $\text{km}^2$ ) for each glacier and for each stream class. To obtain glacier surface area for 1959 and 2020, we used the Randolph Glacier Inventory v7 outlines, which were manually corrected at glacier margins and drainage divides using the same ArcticDEM strips employed to create the hillshade models (Table A3). These strips were then clipped to match the extent of each glacier outline, and elevation polygons were generated at 100 m increments for both years to calculate PTL and  $D_d$  by elevation. PTL highlights channel type distributions independently of length changes, allowing for year-to-year comparisons.

Sinuosity, the ratio of channel length to straight-line distance, was also calculated for canyons on each glacier. Incised and surface channels were excluded due to their narrow width and/or transient nature, making consistent mapping difficult. The straight-line distance was drawn following the valley centerline (midpoint between channel walls), capturing directional changes along different reaches. The Mann–Whitney U test with a statistical significance level of  $p < 0.05$  and boxplots were then used to assess whether sinuosity distributions statistically differed between years.

### 3.8. Moulins and sink points

Moulins typically require substantial and consistent water input, making them hydrologically significant when connected to active perennial supraglacial channels (Bash and others, 2023). Similarly, crevasses can disrupt supraglacial drainage by capturing channel flow, storing water or transferring it to the other glacial hydrological subsystems (St Germain and Moorman, 2019). Due to the difficulty of differentiating these features in satellite and aerial imagery, both hydrologically significant moulins and crevasses are referred to as sink points in this study. These were manually identified where channels terminated abruptly in the 1959 aerial photographs and

2020 PlanetScope imagery. The higher resolution of the historical aerial photographs often allowed direct identification of moulins as rounded, tone-distinct features, beyond which channels did not extend, which was not always possible in the PlanetScope imagery. To address this, manual validation was conducted on two glaciers using the high-resolution (0.5 m) panchromatic WV2 and WV3 images from summer 2022, covering the ablation area of Unnamed 2 Glacier and all of Unnamed 1 Glacier (Table A2).

### 3.9. Surface mass balance

To better understand the drivers behind the changes observed in various supraglacial systems, we utilized the daily modeled SMB dataset for the northern Canadian Arctic Archipelago from Noël and others (2018), updated to cover the period 1959 to 2020. SMB estimates are derived from the 11 km resolution regional climate model RACMO2.3, by summing individual daily components (precipitation, melt, runoff, refreezing, sublimation and drifting snow erosion). These outputs are then statistically downscaled to a finer 1 km resolution to better capture smaller ice masses. For additional information on the downscaling procedure, see Noël and others (2018).

In the current study, the 2020 ELA was used to divide the glaciers into their ablation and accumulation areas, and the specific SMB was calculated separately for each.

## 4. Results

### 4.1. Contemporary drainage patterns

The supraglacial drainage system of glaciers north of Sydkap generally follows a similar pattern, where channels are not clearly defined in areas of high topographic variability, such as within accumulation zones. Instead, they form a broad dendritic drainage network primarily composed of smaller streams and incised rivers with some terminating in sinks on both Unnamed 2 and John Evans (Fig. 3). Smaller streams and rivers that do progress down-glacier transition into sub-parallel configurations before converging into larger, entrenched incised rivers, which eventually develop into canyons flowing parallel to the glacier's direction of flow, a pattern particularly evident on Henrietta–Nesmith Glacier (Fig. 3b). Smaller dendritic and sub-parallel tributary systems, primarily composed of streams and incised rivers, flow alongside these main channels, such as on Unnamed 1 Glacier where they cover most of the surface. This pattern is especially pronounced given that Unnamed 1 no longer possesses a distinct accumulation zone (Fig. 3a).

In the ablation zones of both Unnamed 2 and John Evans glaciers, where most of the supraglacial drainage system is concentrated (84.7% and 62.5%, respectively), meltwater transport is disrupted by prominent sink fields. These features, located at approximately 740 m elevation on Unnamed 2 and 600 m on John Evans, intercept flow from major supraglacial rivers, preventing continuous downstream transfer of meltwater from the upper to the lower ablation areas. In these lower sections, channels eventually reappear, fed by other streams and rivers originating from the southern portions of the glaciers' accumulation areas (Fig. 3c and d). While a limited number of channels, particularly rivers, terminate in sinks near the mapped glaciers' termini (only one sink on Unnamed 1), most flow off the glaciers' surfaces (Fig. 3).

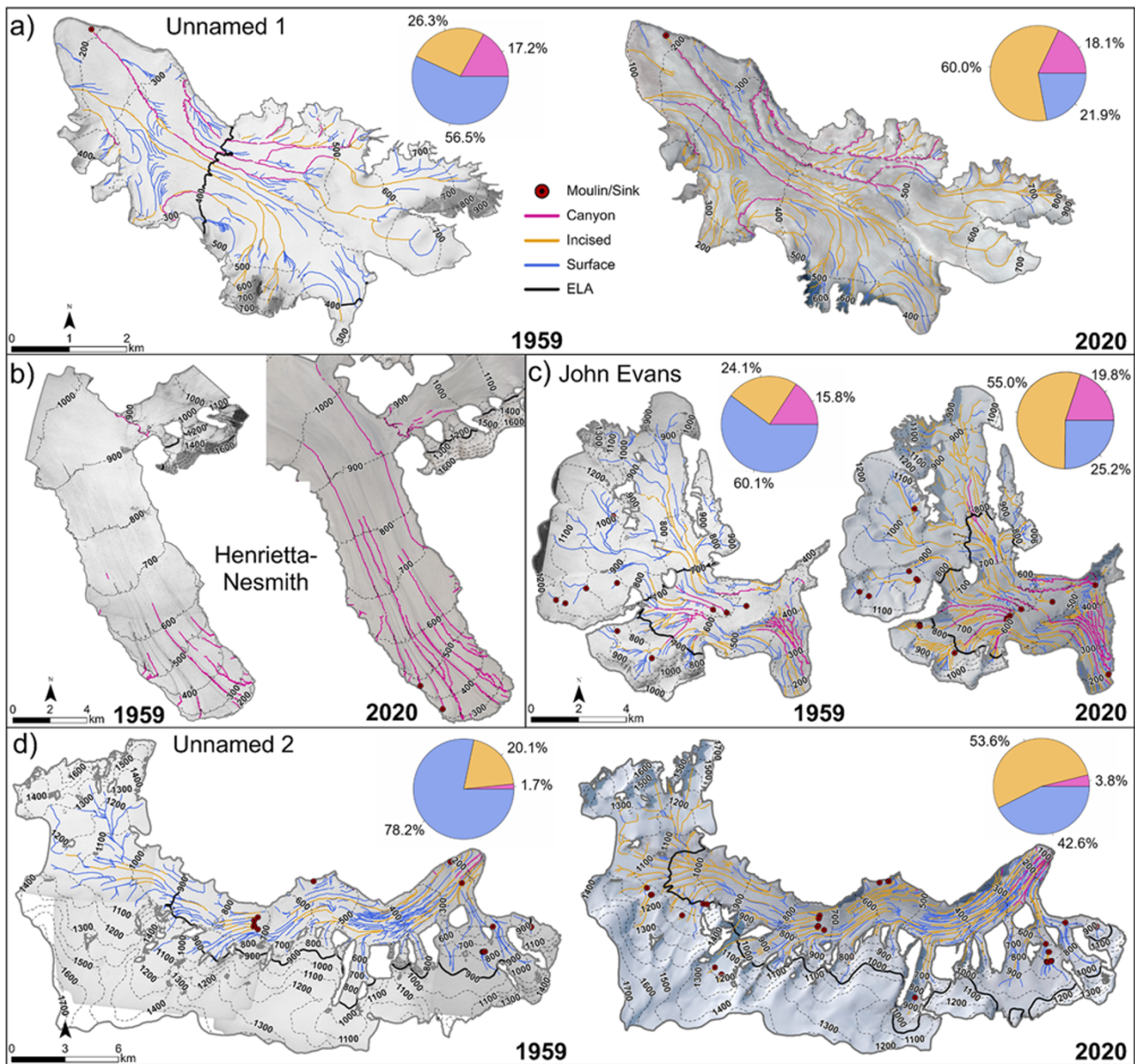


**Figure 3.** Canyon, incised and surface channels, along with sink areas, on (a) Unnamed 1 Glacier, (b) Henrietta-Nesmith Glacier, (c) John Evans Glacier and (d) Unnamed 2 Glacier, delineated on historical aerial photographs from 1959 and PlanetScope images from 2020. The solid black line represents the estimated ELAs for 1959 and 2020 (Note: no ELA is shown for Unnamed 1 in 2020 as it is now above the highest elevation of the glacier). The pie charts indicate the percentage contribution of each channel class to the total channel length in both years.

#### 4.2. Qualitative multi-decadal changes

The qualitative time series analysis reveals substantial changes in the supraglacial hydrological networks of the studied glaciers over the past ~60 years, with trends indicating a recent shift towards more established perennial drainage systems. These changes are observed in various aspects such as the number (e.g. Fig. 4 and Fig. B1 in Appendix B), length (e.g. Fig. 4), width (e.g. Fig. 4, Fig. B2 in Appendix B and Fig. 5), incision (e.g. Fig. 5) and sinuosity of the channels (e.g. Figs. B1 and B2), with some changes accelerating in the last decade. Additionally, some perennial channels have extended further up-glacier over the study period (e.g. Fig. 4 and Figs. B1 and B2).

John Evans Glacier exemplifies many of these changes. For example, a new perennial river formed in the northern part of

the ablation area of the glacier between 1959 and 1987 (Fig. 4b and c). Channels have also lengthened over time, such as one channel that extended from the upper ablation area to lower elevations, connecting the upper supraglacial system with the system located in the terminus region (dots in Fig. 4e-f). This channel extended by ~0.3 km between 1959 and 1987, barely extended between 1987 and 2002, extended by ~0.5 km between 2002 and 2011, and eventually reached the downstream system sometime between 2011 and 2020. Channel banks and valley walls have also widened over time, especially along the now larger canyon rivers. For example, between 1959 and 2020, the channel cross-sections represented by the orange and pink lines widened by several tens of meters (~99 and 34 m, respectively). In addition, larger rivers have increased in importance in the southern portion of the accumulation area, especially since the early 2010s (Fig. 4e and f).

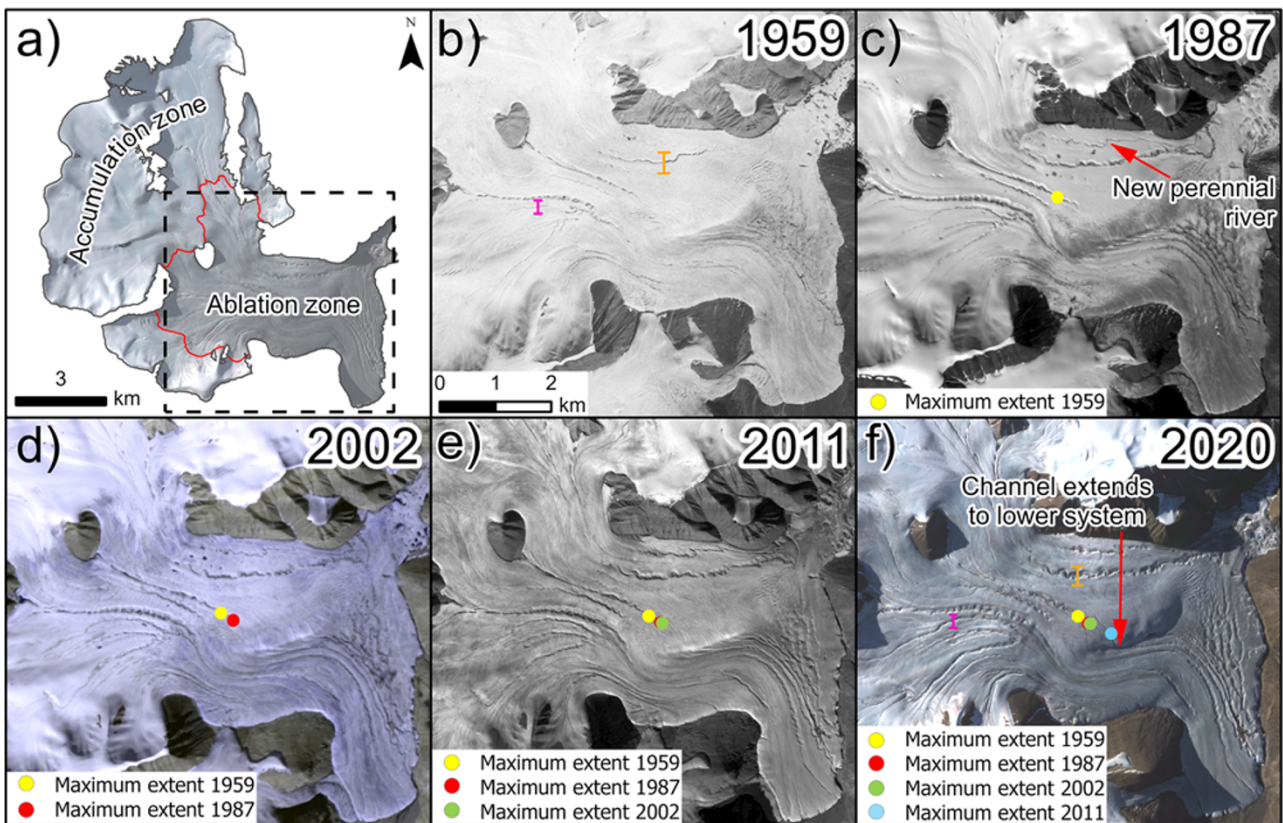


**Figure 4.** Channel evolution on John Evans Glacier between 1959 and 2020. (a) Overview of the glacier, with the ablation area shown in panels (b–f) outlined by the black box. The red line represents the estimated 2020 ELA at  $789 \pm 52$  m a.s.l. (b)  $\sim 0.6$  m resolution historical aerial photo, (c) 20 m resolution SPOT-1 image, (d) 15 m resolution ASTER image, (e) 5 m resolution SPOT-5 image, (f) 3 m resolution PlanetScope image. Colored dots show down-glacier progression of a channel over time and orange/pink cross-section lines in 1959 and 2020 mark the area where channel width was compared over time. See Tables A1 and A2 for image dates.

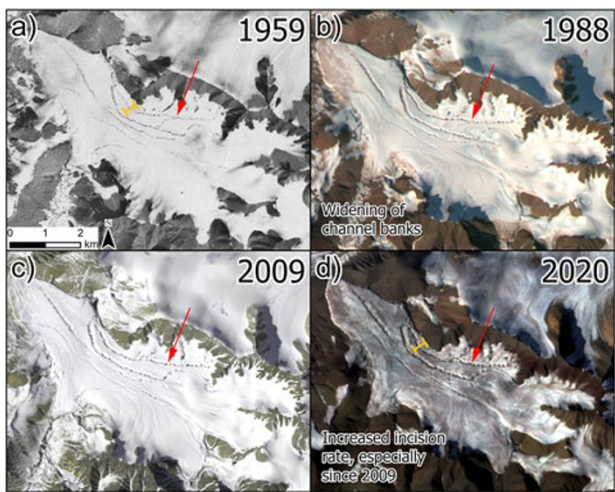


**Figure 5.** Channel evolution on Unnamed 1 Glacier between 1959 and 2020. (a)  $\sim 4$  m resolution historical aerial photo, (b) 20 m resolution SPOT-1 image, (c) 15 m resolution ASTER image, (d) 3 m resolution PlanetScope image. The red arrow is at the same location in each image and marks a canyon river that has seen particularly important changes in width and incision, with an increase in incision rate over the last decade. The orange cross-section line marks the area where channel width was compared over time. See Tables A1 and A2 for image dates.

On the northern Prince of Wales Icefield, Unnamed 2 Glacier has experienced significant changes in its supraglacial drainage

network over time, particularly in channel sinuosity near the terminus. In this area, larger meanders have developed and subsequently cut through their necks, indicating dynamic channel evolution. As a result, channel banks have widened considerably (e.g. by 90 m since 1959 at the orange cross-section on the main channel near the terminus; Fig. B2b in Appendix B). Such changes are apparent in the main canyon at the terminus in the early 1990s but appear to have accelerated in the 21st century, especially with the expansion of additional canyons (Fig. B2). On Henrietta-Nesmith Glacier, channel dynamism is also observed within older, larger perennial canyons. These large rivers have also extended up-glacier, and numerous new perennial channels have emerged near and within the terminus region, especially since the start of the 21<sup>st</sup> century (see arrows in Fig. B1 in Appendix B). In far northern regions, such as Unnamed 1 Glacier, incision and channel bank widening have become increasingly pronounced across much of the glacier, particularly over the past decade, with canyon valley width approximately increasing by 77 m along the orange-marked cross-section since 1959 (Fig. 5).

In contrast to the other glaciers, the supraglacial hydrology of Sydkap Glacier has exhibited a different temporal evolution. A large crevasse field dominates the terminus region and extends  $\sim 7.5$  km up-glacier, inhibiting the formation of a perennial hydrological system (Fig. 6b). Further up-glacier, channels have remained poorly defined throughout the study period, indicating that they may change their course frequently (Fig. 6c–f). Only near the equilibrium line and within the accumulation area are

larger channels found, but these disappear relatively quickly as they progress down-glacier, terminating in sinks, crevasses or smaller distributed systems (Fig. 6d–f).

#### 4.3. Quantitative drainage system evolution between 1959 and 2020

Since 1959, the general structure of the supraglacial drainage systems has remained similar (i.e. dendritic networks at higher elevations feeding more streamlined systems at lower elevations), but each system has expanded, particularly into accumulation areas (Fig. 3). Over the past  $\sim$ 60 years, total channel length and consequently total  $D_d$ , have increased across all glaciers. By 2020, Unnamed 2 and John Evans Glacier had total channel lengths of  $474 \pm 1.3$  km and  $283 \pm 1.4$  km, respectively, reflecting increases of  $35.8\% \pm 0.4\%$  and  $39.4\% \pm 0.7\%$  since 1959. In contrast, Unnamed 1 Glacier, the northernmost, saw a modest  $7.1\% \pm 0.8\%$  increase to  $106 \pm 0.8$  km. Consequently, total  $D_d$  rose from  $1.38 \pm 0.001$ ,  $2.45 \pm 0.002$  and  $5.21 \pm 0.01$  in 1959, to  $1.96 \pm 0.01$ ,  $3.57 \pm 0.02$  and  $5.83 \pm 0.04$  km  $\text{km}^{-2}$  in 2020 on these three glaciers, respectively, with  $D_d$  remaining lowest on Unnamed 2 and highest on Unnamed 1 over the years (Fig. 7). Henrietta-Nesmith Glacier also experienced drainage system expansion, with total canyon length increasing by  $204.8\% \pm 1\%$  to 128 km by 2020.

The relative contribution of channel classes to the total length has also shifted across all glaciers towards increased channelization and incision (Fig. 7). In 1959, surface streams accounted for approximately 78.3%, 60.2% and 56.8% of the total channel length on Unnamed 2, John Evans and Unnamed 1 glaciers, respectively. By 2020, incised rivers had become the dominant channel type, comprising approximately 53.6%, 54.9% and 60.0% of the total length. Canyons, which only made up approximately 1.6%, 15.8% and 17.0% of the total length of channels on these glaciers in 1959, made up approximately 3.9%, 19.9% and 17.9% by 2020 (pie charts in Fig. 3).

While the overall trend of changing channel types is evident across all three glaciers, the absolute rate and relative shift toward a more perennial drainage system vary between them. On Unnamed 2 Glacier, canyon length tripled from  $6 \pm 0.03$  km in 1959 to  $18 \pm 0.4$  km in 2020, expanding at an average rate of approximately  $0.20 \pm 0.01$  km  $\text{a}^{-1}$ . However, canyons still contribute less to the total channel length compared to Unnamed 1 Glacier, despite the latter experiencing a slower growth rate of  $0.03 \pm 0.003$  km  $\text{a}^{-1}$  (pie charts in Fig. 3). A similar pattern is observed for incised rivers on these two glaciers, contributing to the persistence of perennial features, defined here as the combined length of canyons and incised rivers, which remains highest on Unnamed 1 Glacier compared to all other glaciers. Although John Evans and Henrietta-Nesmith Glaciers exhibited higher absolute rates of canyon expansion ( $0.39 \pm 0.003$  and  $1.41 \pm 0.01$  km  $\text{a}^{-1}$ , respectively) than Unnamed 2, their relative increases were still lower in comparison.

##### 4.3.1. Spatiotemporal variability of supraglacial channels

Between 1959 and 2020, total  $D_d$  increased across all elevations on both John Evans Glacier and Unnamed 2 Glacier, with the most pronounced rise occurring within the first 300 m bands from the terminus (Fig. 8c, d, g and h). In contrast, on Unnamed 1 Glacier, the most significant changes occurred above the 1959 ELA, beyond 400 m, with peak total  $D_d$  shifting to a higher elevation (Fig. 8a and e).

These changes in total  $D_d$  are primarily driven by the development and expansion of perennial (incised) channels, as surface stream  $D_d$  has decreased across all glacier surfaces (Fig. 8). On Unnamed 2 Glacier, the PTL of canyons, which was previously concentrated within the 100 m band, is now more evenly distributed between the 100 and 200 m bands (Fig. 9d and h), with canyon  $D_d$  increasing across all bands up to 500 m, where they were previously absent (Fig. 8d and h). Incised rivers are also more prominent at higher elevations, with a particularly pronounced increase in their PTL observed between the 600 and 800 m bands by 2020 (Fig. 9d and h). Their  $D_d$  has increased substantially at and beyond the 800 m band, with rivers extending up-glacier past their 1959 maximum extent within the 1100 m band, to now reach the 1400 m band (Fig. 8d and h).

A similar trend is evident on John Evans Glacier, where canyon distribution has expanded, and  $D_d$  has increased between the 100 and 700 m bands and into the 800 m band where they were previously absent (Fig. 8c and g). Incised rivers, which had a PTL formerly concentrated in the 600 m band, now peak within the 800 m band, with their maximum elevation extending from the 900 to 1100 m band by 2020 (Fig. 9c and g). The  $D_d$  of incised rivers has nearly doubled or more between the 400 and 900 m bands, with the most pronounced increases occurring in the upper ablation zone near 700 m (Fig. 8c and g).

Henrietta-Nesmith Glacier exhibits a comparable pattern, with canyon length extending from a maximum elevation within the 800 m band in 1959 to the 1100 m band in 2020 (Fig. 9b and f). Concurrently, peak  $D_d$  has shifted from the 200 to 400 m band, reflecting the overall increase across all elevation bands (Fig. 8b and f).

As a result, canyons have expanded across a broader elevation range on these three glaciers compared to 1959, now dominating the lower ablation areas. Meanwhile, incised rivers have become more prevalent further up-glacier, with peak  $D_d$  values shifting to higher elevations.

In contrast to these glaciers, Unnamed 1 Glacier exhibits more limited changes in canyon distribution (PTL) (Fig. 9a and e), despite a rise in  $D_d$  at almost all elevations and a threefold rise in the 500 m band (Fig. 8a and e). Similarly, the  $D_d$  of incised rivers has more than doubled across much of the glacier, with the most notable increases occurring beyond the 1959 ELA, which has now retreated beyond the glacier's highest elevation (Fig. 8a and e). This channel class now dominates most of the glacier's surface, even in elevation bands where canyons are most abundant.

##### 4.3.2. Changes in sinuosity

In 1959, sinuosity values were generally higher for most glaciers, except for John Evans, compared to 2020. This is particularly evident on Unnamed 1 Glacier, where the median, interquartile range and a single outlier from 1959 show substantially higher sinuosity values than those recorded in 2020 (Fig. 10). Despite the overall decrease, some glaciers exhibit considerable variability, with multiple outliers in both years indicating sporadic instances of higher sinuosity. This variability is especially notable for glaciers other than Unnamed 1, where the number of outliers increased, and maximum values rose for Unnamed 2 and John Evans (Fig. 10). Interquartile ranges for 1959 are larger for northern glaciers (Henrietta-Nesmith, Unnamed 1), while southern glaciers (Unnamed 2, John Evans) show increased variability in 2020, indicating a trend towards greater variability in the south and reduced variability in the north (Fig. 10). Despite these observations,  $p$  values do not yield statistically significant results when comparing the distributions of sinuosity values in 1959 and 2020.

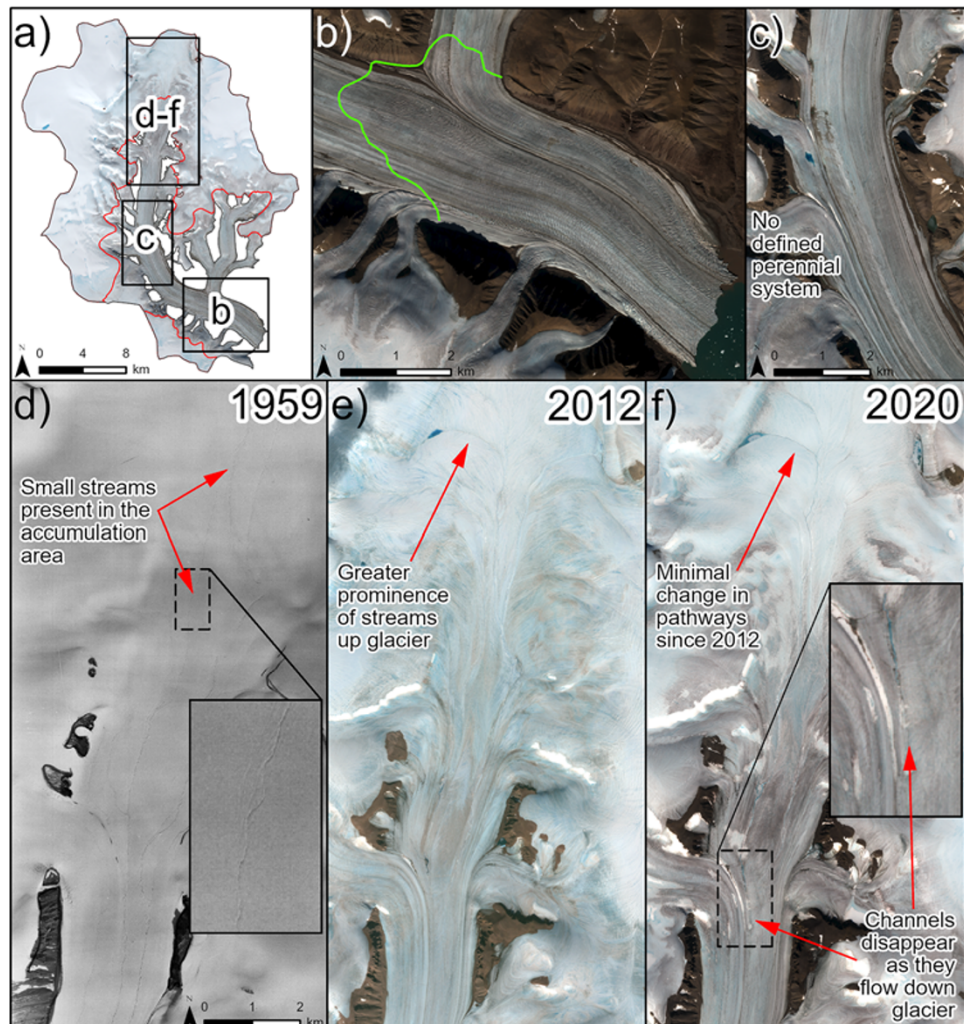


**Figure 6.** (a) PlanetScope image of Sydkap Glacier, showing the absence of a perennial supraglacial drainage system; boxes indicate the location of images in (b–f), and the red line represents the estimated 2020 ELA at  $831 \pm 32$  m a.s.l. (b) Close-up of the terminus, highlighting the upper limit of the crevasse field (green line), which inhibits the uninterrupted transport of meltwater across the glacier surface  $\sim 7.5$  km from the terminus. (c) Close-up showing an area further up-glacier, where supraglacial channels remain limited even in the absence of crevasses. (d–f) Channel evolution in the accumulation area of Sydkap Glacier from 1959 ( $\sim 4$  m resolution historical aerial photo) to 2012 (10 m resolution SPOT-5 image) to 2020 (10 m resolution Sentinel-2 image). See Tables A1 and A2 for image dates.

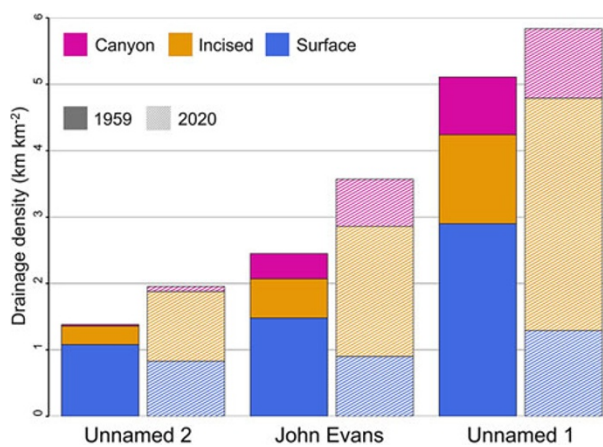


**Figure 7.** Contribution of each channel class to the total drainage density ( $D_d$ ;  $\text{km km}^{-2}$ ) for each glacier for the years 1959 and 2020.

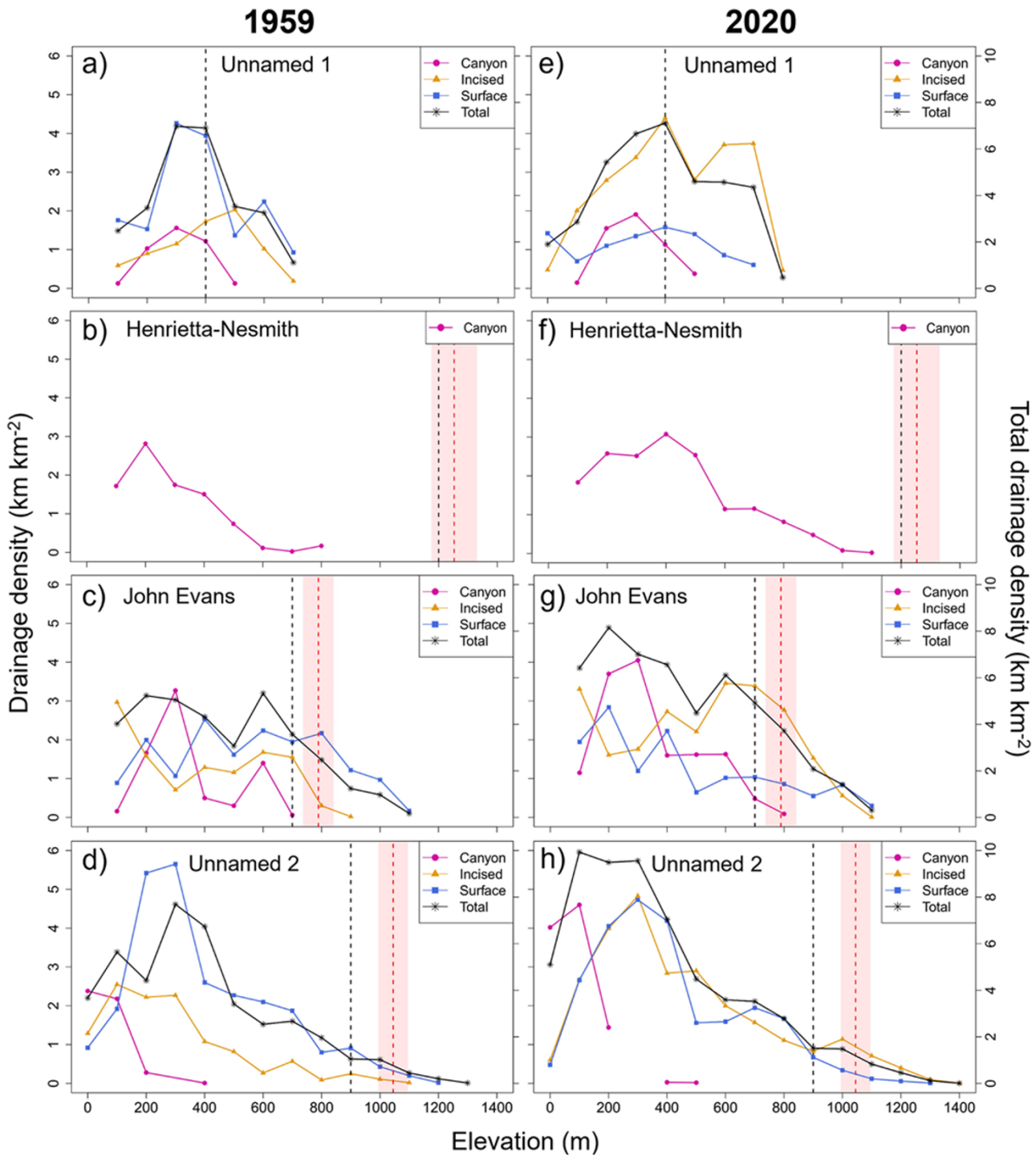


**Figure 8.** Drainage density ( $D_d$ ;  $\text{km km}^{-2}$ ) by channel class as a function of elevation for the four mapped glaciers in 1959 and 2020. Total  $D_d$  combining all classes (black solid line) is shown on the secondary axis. Graphs are organized by latitude based on the location of each glacier: (a and e) Unnamed 1, (b and f) Henrietta-Nesmith, (c and g) John Evans and (d and h) Unnamed 2. Elevation is capped at 1400 m, which represents the highest elevation band at which channels were mapped. The black and red dotted lines show the position of the 1959 and 2020 ELAs, respectively, with the red shaded areas representing the uncertainty range for the 2020 ELAs. No ELA is shown for Unnamed 1 in 2020 as it is now above the highest elevation of the glacier at  $\sim 980$  m a.s.l.

#### 4.4. Changes in SMB

Modeled monthly specific SMB for the ablation areas of the five studied glaciers reveals significant trends in mass losses since the mid-1960s ( $p < 0.05$ ) (Fig. 11a–e and Table C1 in Appendix C). These losses are primarily associated with the melt season,

which typically occurs from June to August. Since the mid-1960s, snowfall (i.e. SMB gains) in the ablation areas of the five studied glaciers have shown generally low variability (Fig. 11a–e), with significant decreases observed only on Sydkap and Henrietta-Nesmith (Table C1).

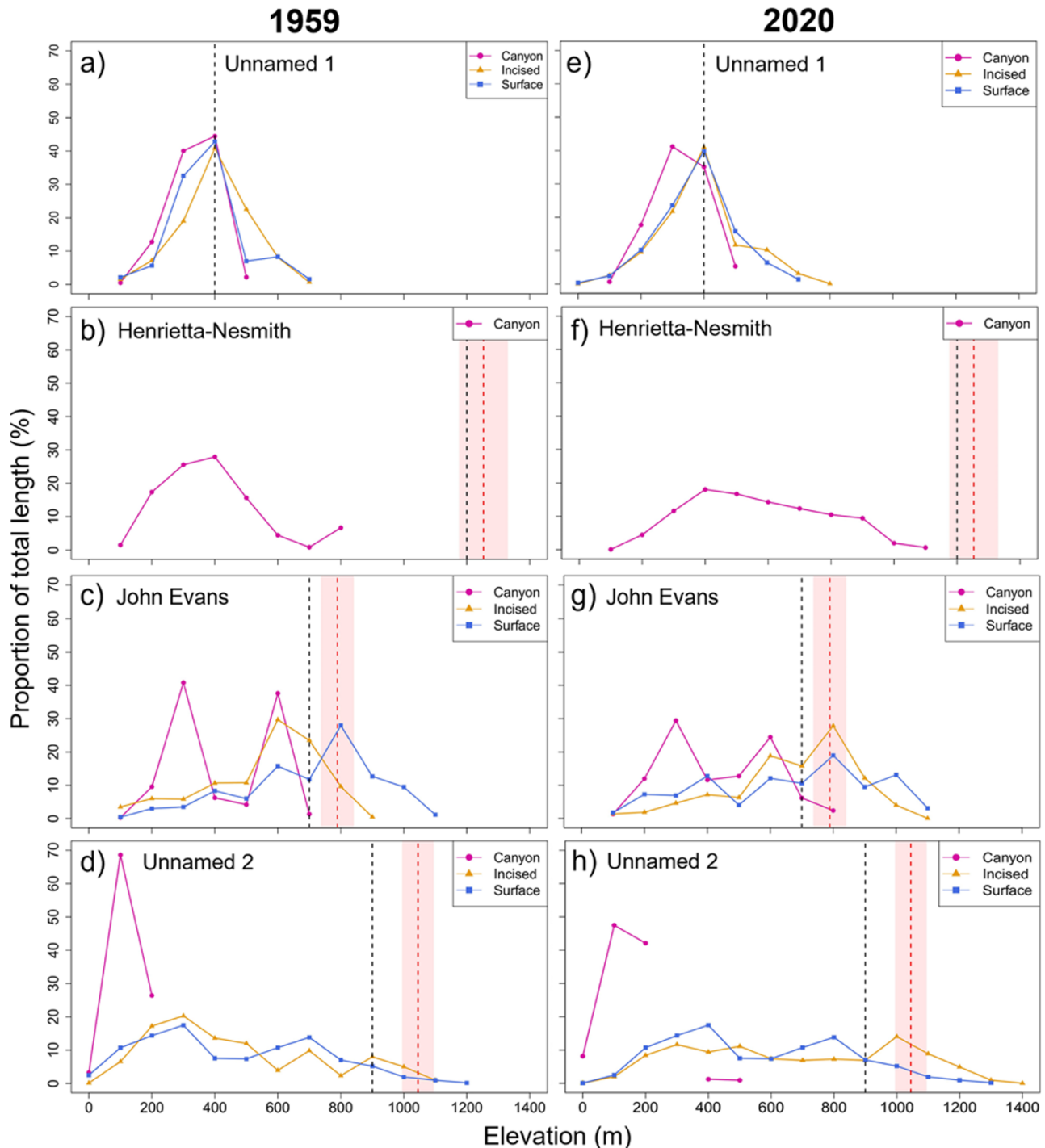


**Figure 9.** Proportion of total length (PTL; %) by channel class as a function of elevation for the four mapped glaciers in 1959 and 2020. Graphs are organized by latitude based on the location of each glacier: (a and e) Unnamed 1, (b and f) Henrietta-Nesmith, (c and g) John Evans and (d and h) Unnamed 2. Elevation is capped at 1400 m, which represents the highest elevation band at which channels were mapped. The black and red dotted lines show the position of the 1959 and 2020 ELAs, respectively, with the red shaded areas representing the uncertainty range for the 2020 ELAs. No ELA is shown for Unnamed 1 in 2020 as it is now above the highest elevation of the glacier at  $\sim 980$  m a.s.l.

All glaciers show a significant negative trend in net annual specific SMB, with mass losses increasing between 48.14% and 127% between the periods 1964–99 and 2000–20 in the ablation area of all studied glaciers (Fig. 11a–e and Table 2). The magnitude and rate of these losses vary by latitude, with the highest values observed on Sydkap Glacier (furthest south) and the lowest

on Unnamed 1 Glacier (furthest north) (Fig. 11a–e and Table C1). Cumulative summer SMB losses between 1964 and 2020 reached  $-51.45$  m w.e. on Sydkap compared to  $-23.72$  m w.e. on Unnamed 1 (Fig. 11a and e). Linear regression slopes also highlight this contrast, indicating faster loss rates on Sydkap ( $-13$  mm w.e.  $a^{-1}$ ) than on Unnamed 1 ( $-6.24$  mm w.e.  $a^{-1}$ ) (Table C1).

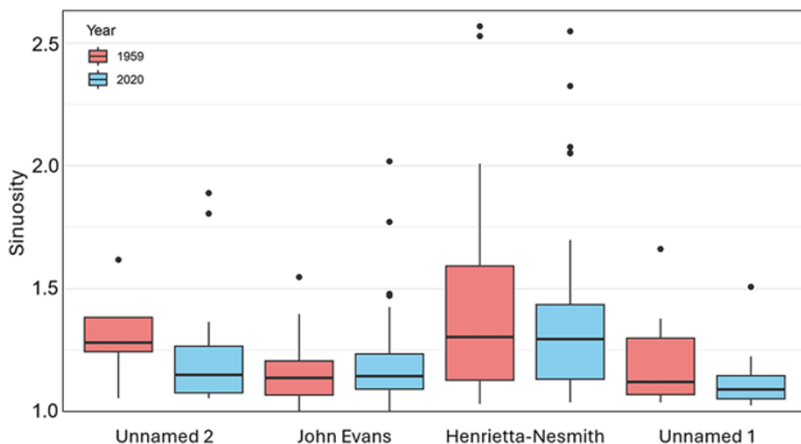


**Figure 10.** Box plot showing the median, interquartile range and outlier sinuosity values for Unnamed 2, John Evans, Henrietta-Nesmith and Unnamed 1 glaciers for 1959 and 2020.

**Table 2.** Average losses ( $\text{mm w.e. a}^{-1}$ ) used as a proxy for surface melt across the ablation (Ab) and accumulation (Ac) areas of the five studied glaciers over the 1959–2020 period, derived from the regional climate model RACMO2.3

Year	Unnamed 1		Henrietta-Nesmith		John Evans		Unnamed 2		Sydkap	
	Ab	Ac	Ab	Ac	Ab	Ac	Ab	Ac	Ab	Ac
1960s	-482	N/A	-409	-12.50	-817	-299	-632	-128	-939	-208
1970s	-332	N/A	-267	-2.49	-549	-99.70	-407	-37.60	-721	-112
1980s	-307	N/A	-319	-3.84	-708	-288	-536	-88.70	-860	-180
1990s	-324	N/A	-365	-5.19	-747	-294	-582	-94.80	-839	-175
2000s	-555	N/A	-591	-18.80	-952	-403	-734	-142	-1021	-260
2010s	-553	N/A	-746	-50.30	-976	-516	-902	-325	-1288	-389
1964–99 average	-325	N/A	-305	-3.28	-645	-200	-492	-66.50	-757	-134
2000–20 average	-572	N/A	-693	-37	-955	-450	-832	-242	-1152	-323

In the accumulation area, losses also exhibit a significant negative trend from 1964 to 2020 ( $p < 0.05$ ), with mass gains also showing significant negative trends on some glaciers (Fig. 11f–i and Table C1). However, losses are increasing at a much faster rate than gains are decreasing (Fig. 11f–i and Table C1). Between 1964–99 and 2000–20, accumulation area losses more than doubled on Sydkap and John Evans, more than tripled on Unnamed 2, and increased over elevenfold on Henrietta-Nesmith (Table 2). These relative changes in losses are much greater in the accumulation areas compared to their respective ablation zones, highlighting the increasing vulnerability of higher-elevation regions (Table 2).

Following this pattern of increasing losses, the ELA has risen on all mapped glaciers since 1959, though the magnitude of change varies considerably. On northern Ellesmere Island, the ELA now lies above the highest point of Unnamed 1 Glacier, an increase of more than 580 m a.s.l., effectively eliminating its accumulation zone (Fig. 12a). On Henrietta-Nesmith Glacier, the ELA rose by approximately  $53 \pm 77$  m between 1959 and 2020, yet the impact on its Accumulation Area Ratio (AAR) was minimal, which remains high at  $\sim 0.81$  (Fig. 12b) (Dyurgerov and others, 2009). Further south, John Evans and Unnamed 2 glaciers experienced ELA increases of  $89 \pm 52$  and  $145 \pm 50$  m, respectively, resulting in notable AAR reductions of  $\sim 12.5\%$  and  $\sim 20.2\%$  (Fig. 12c and d).

## 5. Discussion

### 5.1. Supraglacial drainage systems

Studies on supraglacial drainage patterns in the northern Canadian Arctic Archipelago remain limited. However, Lu and others (2020) reported patterns similar to those observed in this study on Devon Ice Cap, where high-elevation supraglacial channels formed broad

dendritic networks that became increasingly channelized and subparallel at lower elevations, eventually developing into regularly spaced, parallel mainstems within outlet glacier trunks. Consistent with our findings and studies on polythermal glaciers in the northern and southern Canadian Arctic Archipelago, Greenland and Svalbard (Rippin and others, 2015; St Germain and Moorman, 2016, 2019; Yang and others, 2019; Lu and others, 2020), sinuosity was highest within the mainstems and increased towards the glacier terminus. Charlton (2007) notes that natural rivers adjust their slope, typically decreasing it, by increasing sinuosity. On Fountain Glacier, Bylot Island, St Germain and Moorman (2019) found that supraglacial channels remained relatively straight until reaching the sloped terminus, where lateral meanders developed at rates of  $0.2\text{--}1.9 \text{ m a}^{-1}$ , depending on channel size.

Although our study did not specifically examine meander growth, sinuosity values for canyon rivers show no significant pattern of change over the study period. This likely reflects the dynamic nature of these channels: continuous bank erosion from melting leads to meander cutoffs and channel straightening, after which new meanders begin to form as the channels readjust their slope (Rippin and others, 2015; St Germain and Moorman, 2019). This process is clearly visible in the time series for Unnamed 2 through Henrietta-Nesmith glaciers (Figs. 4, 5, B1, B2). This is supported by St Germain and Moorman (2019), who show that canyon sinuosity is strongly correlated with slope and watershed area, which influence discharge and cause meander development rates to vary between canyons.

#### 5.1.1. System evolution

While drainage patterns were broadly consistent across glaciers and over time, total channel length and  $D_d$  differed significantly, with the highest  $D_d$  on the northernmost glacier (Unnamed 1) and

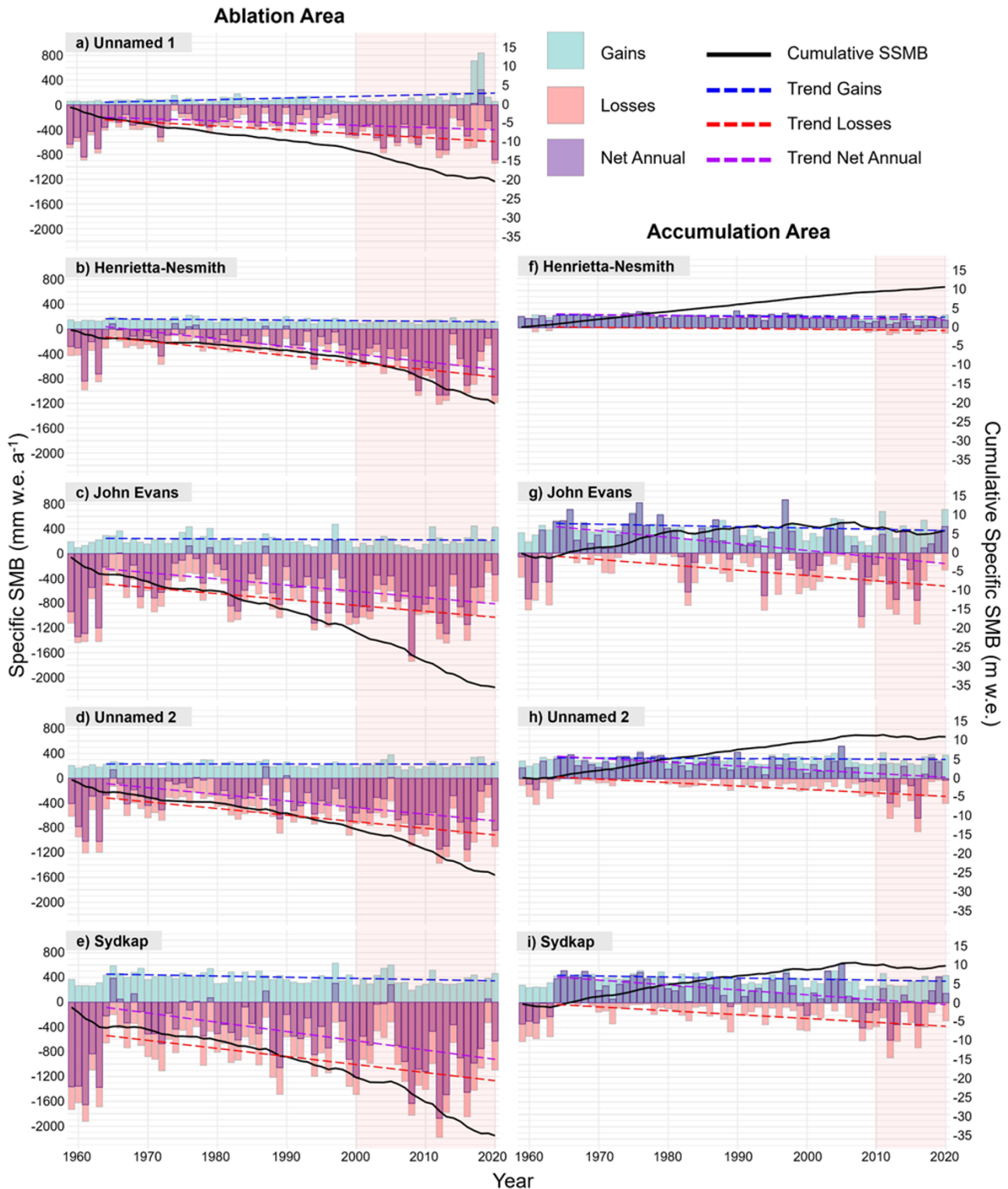


**Figure 11.** Annual surface mass balance (SMB) components for the ablation (a-e) and accumulation (f-i) areas of the five studied glaciers from 1959 to 2020: Gains (blue), losses (pink) and net annual (purple), with trendlines from 1964 depicted in dark blue (gains), red (losses) and violet (net annual). Cumulative net specific SMB (SSMB; black solid line) is shown on the secondary axis. SMB values were derived from the regional climate model RACMO2.3 downscaled to 1 km resolution, and specific glacier values were computed by summing all raster values within the glacier area and dividing by the glacier's surface area.

the lowest on the southernmost (Unnamed 2) in both 1959 and 2020 (Fig. 7). Glaciers with extensive cold ice are less dynamic and have smoother, less crevassed surfaces, limiting surface

meltwater access to englacial and subglacial pathways (Rippin and others, 2015). As a result, supraglacial channels on such glaciers are often widespread, draining meltwater over large areas

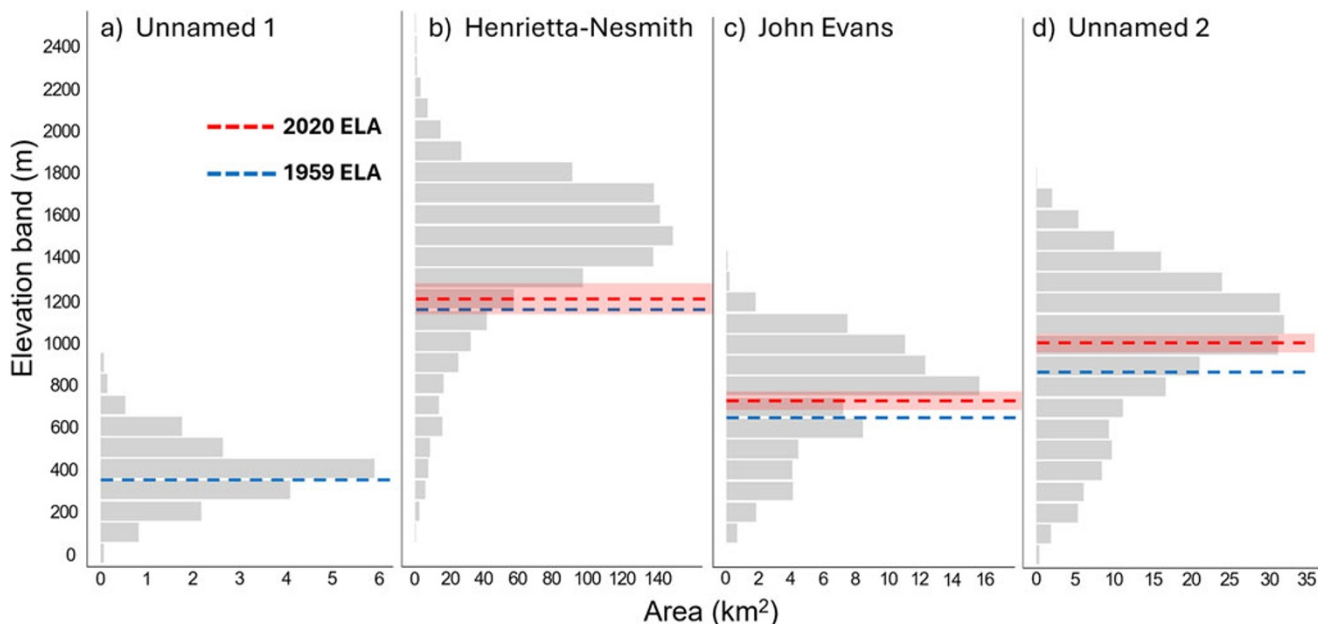


**Figure 12.** Glacier hypsometry for (a) Unnamed 1, (b) Henrietta-Nesmith, (c) John Evans and (d) Unnamed 2 glaciers. The ELA for each glacier in 1959 and 2020 is shown as the blue and red dashed lines, respectively, with the red shaded areas representing the uncertainty range for the 2020 ELAs. Only the 1959 ELA is included for Unnamed 1 as the highest point on this glacier is now below the regional ELA.

(Irvine-Fynn and others, 2011; Ryser and others, 2013; Rippin and others, 2015). Bash and others (2023) found that channels were 98% more common on Thores Glacier on Northern Ellesmere Island, where ice is likely frozen to the bed (Kochtitzky and others, 2023), than on Nàludäy (Lowell Glacier) in the Yukon, suggesting broader channel development on colder ice masses, consistent with this study. In addition, no moulin were found on Thores Glacier (Kochtitzky and others, 2023), consistent with our observations that prominent sink fields were present on both Unnamed 2 and John Evans glaciers to the south, whereas only limited sinks were mapped on Henrietta-Nesmith and Unnamed 1 to the north (Fig. 3).

This pattern echoes findings by Yang and others (2019), who noted that moulin are rare in northwest Greenland but vital to supraglacial drainage in the southwest, attributing this difference to colder, thicker and less permeable ice in the north, along with slower flow and lower strain rates. Similar conditions may explain their absence on northern glaciers in our study area, as Kochtitzky and others (2023) reported nearby Thores Glacier to be slow-moving and cold-based, with modeled basal temperatures ranging from  $-7^{\circ}\text{C}$  to  $-12^{\circ}\text{C}$ . Previous research on John Evans Glacier has shown that sink fields are linked to seasonal increases in surface motion, highlighting its sensitivity to variations in surface meltwater input (Bingham and others, 2003). The emergence of new sinks in the western accumulation area of Unnamed 2 Glacier suggests the development of a subglacial drainage system, which could lead to enhanced basal flow (Fig. 3d). At a similar latitude on Axel Heiberg Island, Thomson and Copland (Thomson and Copland, 2017, 2018) observed that the upglacier development of moulin since the 1960s on White Glacier enabled basal sliding to occur at higher elevations than previously recorded. These findings suggest that southern glaciers exhibit stronger hydrological coupling, allowing more meltwater to reach the bed, whereas weaker coupling in northern glaciers retains water at the surface, promoting more widespread supraglacial drainage systems.

While changes in  $D_d$  on Unnamed 2 and John Evans glaciers were primarily driven by increases in total channel length, rather than reductions in glacier area, approximately 50% of the increase in  $D_d$  on Unnamed 1 can be attributed to surface area loss. This aligns with the relatively small increase in channel length on Unnamed 1 and the fact that the glacier now lies entirely within the ablation zone, indicating a negative mass balance across its entire surface (Fig. 3a).

One consistent pattern observed across all glaciers is the shift toward a more perennial drainage system, marked by an increasing contribution of incised rivers and canyons over time (pie charts in Fig. 3). This trend highlights an important transformation: while canyons and incised rivers have long played a significant role at lower elevations, they have become increasingly widespread across the glacier surfaces. This includes canyon development on Henrietta-Nesmith, which has seen an increase in both PTL at higher elevations and  $D_d$  over the study period (Figs. 8b and f and 9b and f).

On Unnamed 1 Glacier, the retreat of the ELA beyond the glacier's highest point likely contributed to a concurrent rise in  $D_d$  and PTL of incised rivers at higher altitudes (Figs. 8a and e and 9a and e). In contrast, John Evans and Unnamed 2 glaciers showed the greatest changes in  $D_d$  at lower elevations, where increases were mainly driven by the rapid expansion of canyon rivers into the upper ablation zone (Fig. 8c, d, g and h). While  $D_d$  did not increase as significantly at higher elevations on John Evans and Unnamed 2, incised rivers still showed substantial development there (Fig. 8c, d, g and h).

Our observations suggest that the surface drainage system of Unnamed 1 Glacier adjusted to prevailing climatic conditions earlier than those of the other glaciers, likely due to its smaller watershed area and already high total  $D_d$  in 1959. This is further supported by the limited increase in total channel length over the study period, as well as the lowest absolute and relative rates of change in perennial rivers observed among all glaciers. These findings

indicate that a well-established supraglacial drainage network was already in place during the earlier period, unlike Unnamed 2 Glacier, which, despite having the lowest total  $D_d$ , exhibits the greatest relative change in perennial rivers, suggesting rapid hydrological reorganization. As with Unnamed 1, the watershed area likely influenced the absolute canyon growth rates on both John Evans and Henrietta-Nesmith glaciers. Henrietta-Nesmith, the largest glacier and John Evans, with its wide ablation zone, have geometries that can potentially support the formation of large individual canyon watersheds, which may enhance meltwater discharge and contribute to canyon development (Fig. 3b and c). These findings suggest that while northern glaciers may exhibit greater stability and higher drainage densities due to broader environmental conditions, glacier-specific characteristics, such as geometry, may play a key role and should be considered in future studies.

Overall, the most prominent changes in incised rivers occurred in the transition zone between ablation and accumulation areas, typified by glaciers Unnamed 2 through Unnamed 1, reflecting the upward shift of the ELA since 1959. This transition has resulted in higher melt rates and increased meltwater availability, promoting enhanced erosion and the formation of new incised rivers throughout this zone, as well as within the initial elevation bands of the accumulation areas, particularly on John Evans Glacier (Fig. 8c and g).

To date, only St Germain and Moorman (2019) have examined the mechanisms driving the development of different supraglacial channel types in the Canadian Arctic Archipelago. Their findings, which align with earlier work by Knighton (1981) in Norway and Marston (1983) in Alaska, indicate that higher meltwater discharge and steeper glacier gradients are strongly associated with faster incision rates. This suggests that the combination of favorable glacier gradients and high discharge over the study period likely facilitated substantial erosion of channel beds and banks, ultimately enabling the formation and expansion of incised rivers and canyons across our studied glaciers.

## 5.2. Hydrological implications of SMB changes

We observe small or insignificant trends in gains in the ablation zones of the studied glaciers since the mid-1960s, suggesting that the overall decline in net annual SMB is primarily driven by heightened summer melt. These intensified melt conditions are reflected in the evolution of the supraglacial hydrological systems, which have developed differently depending on each glacier's melt regime.

In the far northern regions, lower surface melt rates and generally slower rates of change in losses since the mid-1960s have supported the long-term persistence of a well-developed supraglacial drainage system (Rippin and others, 2015) on Unnamed 1. In contrast, the more southerly glaciers, such as on Unnamed 2 and John Evans, have experienced stronger melt intensities that have accelerated supraglacial system development over the past ~60 years (Fig. 11 and Table 2). On Sydkap Glacier, the combination of high surface ablation and extensive crevassing is likely responsible for the lack of a perennial system, as ablation exceeds incision, limiting channel development beyond the crevasse field.

Relative changes in losses have become particularly pronounced in the accumulation areas of the studied glaciers, where mass losses are increasing at a much faster rate than mass gains are declining (Fig. 11f–i and Table C1). This suggests that supraglacial system development at higher elevations is also primarily melt-driven. The accelerated relative rate of change in the accumulation areas,

compared to their respective ablation zones, is consistent with the observed elevation-dependent warming across the glaciated regions of the northern Canadian Arctic Archipelago since the start of the 21st century. Specifically, the linear rate of change of clear-sky mean summer land surface temperature ( $^{\circ}\text{C a}^{-1}$ ) has been 40% greater at elevations above 1000 m a.s.l. and 76.9% greater at elevations above 1400 m a.s.l. (Mortimer and others, 2016).

The accelerating ice loss in the accumulation areas of the studied glaciers underscores their vulnerability and highlights the potential for expansion of supraglacial channel networks at higher elevations. Since 1959, such expansion has been observed through the development of incised rivers in regions that were previously part of the accumulation zone but have since retreated (Fig. 3). Even relatively minor changes in the ELA can shift large portions of glaciers from the accumulation zone to the ablation zone, facilitating the observed growth of the supraglacial channel networks. This demonstrates the high vulnerability of glaciers with large areas at elevations near the ELA and allowed for rapid expansion of the supraglacial drainage system at higher elevations. If the ELA continues to rise at the observed rates for these glaciers, Unnamed 2 is likely to be particularly vulnerable, due to the large amount of ice concentrated between 1000 and 1200 m a.s.l., potentially accelerating the development of perennial supraglacial features over a larger surface area (Fig. 12d). Unnamed 1 Glacier, with its surface already below the regional ELA, is expected to continue retreating and will ultimately disappear, following trends observed in smaller glaciers and ice caps across Ellesmere Island (Serreze and others, 2017; White and Copland, 2018; Medrzycka and others, 2023).

## 5.3. Limitations and future outlook

While this study provides the first multi-decadal perspective on supraglacial drainage evolution in the Canadian Arctic Archipelago, several limitations constrain the interpretation of our results. The most significant is the absence of a DEM for 1959. As a result, channel mapping for that year relied exclusively on image interpretation. Although the high resolution of the historical aerial photographs (~0.6 m) allowed for the distinction between surface and incised channels, thanks to the visibility of clear channel banks, mapping in 1959 was inherently more subjective than in 2020, where DEM-supported hillshade models enhanced our mapping confidence.

A second major limitation is the scarcity of high-resolution imagery between 1959 and 2020, which restricted our quantitative analysis to just those two years. This temporal gap limits our ability to determine what proportion of supraglacial hydrological development reflects sustained decadal trends versus transient surface hydrological conditions driven by year-to-year variations in melt intensity, particularly for the more ephemeral surface streams. Our decadal qualitative analysis helped partially mitigate this uncertainty by documenting general trends in channel expansion and persistence, but higher temporal resolution would enable a more nuanced understanding of when and how key hydrological shifts occurred.

Future research should aim to link hydrological changes to climatic drivers such as temperature gradients, precipitation regimes, glacier elevation and proximity to the coast. Incorporating regional climate datasets and modeling efforts will help refine predictions of how these systems will continue to evolve in a warming Arctic. Moreover, the significant changes in supraglacial systems presented in this study should be examined within the broader context of

glacier dynamics to better understand how glaciers will respond to ongoing and future climatic changes.

## 6. Summary and conclusion

In this study, we provided the first detailed, multi-decadal analysis of supraglacial drainage development on five glaciers across Ellesmere Island, offering insights into long-term hydrological changes in the northern Canadian Arctic Archipelago. Between 1959 and 2020,  $D_d$  increased on glaciers north of Sydkap, primarily due to the expansion of incised and canyon rivers at higher elevations as ELAs retreated up-glacier. These changes reflect a broader reorganization of supraglacial drainage networks, with perennial, incised channels becoming dominant. Nonetheless, variations in the rate of change of supraglacial hydrological systems exist with northern glaciers such as Unnamed 1 displaying a more stable and less dynamic system compared to glaciers further south such as John Evans and Unnamed 2.

Modeled increases in surface melt support these observations, with glaciers at lower latitudes experiencing faster rates of supraglacial system evolution. Despite this, high surface melt rates on Sydkap Glacier combined with heavy crevassing have inhibited the formation of a persistent surface drainage system there. Although Unnamed 1 has maintained a relatively stable drainage system due to lower melt rates and the likely persistence of cold surface ice, the recent rise of its ELA above the glacier's highest elevation signals ongoing retreat and long-term vulnerability. As ELAs continue to rise, glaciers with most of their ice at mid elevations, such as Unnamed 2, are particularly susceptible to rapid hydrological expansion at higher elevations and continued mass loss.

**Acknowledgements.** This research was generously supported by funding from the Natural Sciences and Engineering Research Council (NSERC) of Canada, ArcticNet Network of Centres of Excellence Canada, Northern Scientific Training Program (NSTP), Polar Continental Shelf Program (PCSP), Amundsen Science, Weston Family Foundation, Fonds de Recherche du Québec (FRQ), University of Manitoba and University of Ottawa. We also extend our thanks to the community members of Grise Fiord for their support throughout this research, and to the Nunavut Research Institute for permission to conduct fieldwork. Brice Noël is a Research Associate of the Fonds de la Recherche Scientifique de Belgique—F.R.S.-FNRS.

## References

Bash EA and 6 others (2023) A semi-automated, GIS-based framework for the mapping of supraglacial hydrology. *Journal of Glaciology* **69**(276), 708–722. doi:[10.1017/jog.2022.92](https://doi.org/10.1017/jog.2022.92)

Bergsma BM, Svoboda J and Freedman B (1984) Entombed plant communities released by a retreating glacier at central Ellesmere Island, Canada. *Arctic* **37**(1), 49–52. doi:[10.14430/arctic2162](https://doi.org/10.14430/arctic2162)

Bingham RG, Nienow PW and Sharp MJ (2003) Intra-annual and intra-seasonal flow dynamics of a High Arctic polythermal valley glacier. *Annals of Glaciology* **37**, 181–188. doi:[10.3189/172756403781815762](https://doi.org/10.3189/172756403781815762)

Bingham RG, Nienow PW, Sharp MJ and Boon S (2005) Subglacial drainage processes at a High Arctic polythermal valley glacier. *Journal of Glaciology* **51**(172), 15–24. doi:[10.3189/172756505781829520](https://doi.org/10.3189/172756505781829520)

Bingham RG, Nienow PW, Sharp MJ and Copland L (2006) Hydrology and dynamics of a polythermal (mostly cold) High Arctic glacier. *Earth Surface Processes and Landforms* **31**(12), 1463–1479. doi:[10.1002/esp.1374](https://doi.org/10.1002/esp.1374)

Casey JA and Kelly REJ (2010) Estimating the equilibrium line of Devon Ice Cap, Nunavut, from RADARSAT-1 ScanSAR wide imagery. *Canadian Journal of Remote Sensing* **36**(1), S41–S55. doi:[10.5589/m10-013](https://doi.org/10.5589/m10-013)

Cavaco MA and 6 others (2019) Freshwater microbial community diversity in a rapidly changing High Arctic watershed. *FEMS Microbiology Ecology* **95**(11), fiz161. doi:[10.1093/femsec/fiz161](https://doi.org/10.1093/femsec/fiz161)

Charlton R (2007) *Fundamentals of Fluvial Geomorphology*. Abingdon, Oxon and New York, NY: Routledge.

Copland L, Sharp MJ and Dowdeswell JA (2003a) The distribution and flow characteristics of surge-type glaciers in the Canadian High Arctic. *Annals of Glaciology* **36**, 73–81. doi:[10.3189/172756403781816301](https://doi.org/10.3189/172756403781816301)

Copland L, Sharp MJ and Nienow PW (2003b) Links between short-term velocity variations and the subglacial hydrology of a predominantly cold polythermal glacier. *Journal of Glaciology* **49**(166), 337–348. doi:[10.3189/172756503781830656](https://doi.org/10.3189/172756503781830656)

Curley AN, Kochtitzky WH, Edwards BR and Copland L (2021) Glacier changes over the past 144 years at Alexandra Fiord, Ellesmere Island, Canada. *Journal of Glaciology* **67**(263), 511–522. doi:[10.1017/jog.2021.44](https://doi.org/10.1017/jog.2021.44)

Dyurgerov M, Meier MF and Bahr DB (2009) A new index of glacier area change: A tool for glacier monitoring. *Journal of Glaciology* **55**(192), 710–716. doi:[10.3189/002214309789471030](https://doi.org/10.3189/002214309789471030)

Glen E and 7 others (2025) A comparison of supraglacial meltwater features throughout contrasting melt seasons: Southwest Greenland. *The Cryosphere* **19**(3), 1047–1066. doi:[10.5194/tc-19-1047-2025](https://doi.org/10.5194/tc-19-1047-2025)

Hattersley-Smith G (1961) The ice cover of northern Ellesmere Island. *Annals of the New York Academy of Sciences* **95**(1), 282–289. doi:[10.1111/j.1749-6632.1961.tb50039.x](https://doi.org/10.1111/j.1749-6632.1961.tb50039.x)

Irvine-Fynn TDL, Hodson AJ, Moorman BJ, Vatne G and Hubbard AL (2011) Polythermal glacier hydrology: A review. *Reviews of Geophysics* **49**(4), RG4002. doi:[10.1029/2010RG000350](https://doi.org/10.1029/2010RG000350)

King L, Hassan MA, Yang K and Flowers G (2016) Flow routing for delineating supraglacial meltwater channel networks. *Remote Sensing* **8**(12), 988. doi:[10.3390/rs8120988](https://doi.org/10.3390/rs8120988)

Knighton AD (1981) Channel form and flow characteristics of supraglacial streams, Austre Okstindbreen, Norway. *Arctic and Alpine Research* **13**(3), 295. doi:[10.2307/1551036](https://doi.org/10.2307/1551036)

Kochtitzky W and 6 others (2023) Slow change since the Little Ice Age at a far northern glacier with the potential for system reorganization: Thores Glacier, northern Ellesmere Island, Canada. *Arctic Science* **9**(2), 451–464. doi:[10.1139/as-2022-0012](https://doi.org/10.1139/as-2022-0012)

Koerner RM (1979) Accumulation, ablation, and oxygen isotope variations on the Queen Elizabeth Islands Ice Caps, Canada. *Journal of Glaciology* **22**(86), 25–41. doi:[10.1017/s0022143000014039](https://doi.org/10.1017/s0022143000014039)

Lampkin DJ and VanderBerg J (2014) Supraglacial melt channel networks in the Jakobshavn Isbrae region during the 2007 melt season. *Hydrological Processes* **24**(28), 6038–6053. doi:[10.1002/hyp.10085](https://doi.org/10.1002/hyp.10085)

Lu Y and 7 others (2020) Diverse supraglacial drainage patterns on the Devon Ice Cap, Arctic Canada. *Journal of Maps* **16**(2), 834–846. doi:[10.1080/17445647.2020.1838353](https://doi.org/10.1080/17445647.2020.1838353)

Marston RA (1983) Supraglacial stream dynamics on the Juneau Icefield. *Annals of the Association of American Geographers* **73**(4), 597–608. doi:[10.1111/j.14678306.1983.tb01861.x](https://doi.org/10.1111/j.14678306.1983.tb01861.x)

Medrzycka D, Copland L and Noël B (2023) Rapid demise and committed loss of Bowman Glacier, northern Ellesmere Island, Arctic Canada. *Journal of Glaciology* **69**(276), 997–1010. doi:[10.1017/jog.2022.119](https://doi.org/10.1017/jog.2022.119)

Millan R, Mouginot J and Rignot E (2017) Mass budget of the glaciers and ice caps of the Queen Elizabeth Islands, Canada, from 1991 to 2015. *Environmental Research Letters* **12**(2), 024016. doi:[10.1088/1748-9326/aa5b04](https://doi.org/10.1088/1748-9326/aa5b04)

Miller GH, Bradley RS and Andrews JT (1975) The glaciation level and lowest equilibrium line altitude in the High Canadian Arctic: Maps and climatic interpretation. *Arctic and Alpine Research* **7**(2), 155. doi:[10.2307/1550318](https://doi.org/10.2307/1550318)

Mortimer CA, Sharp M and Wouters B (2016) Glacier surface temperatures in the Canadian High Arctic, 2000–15. *Journal of Glaciology* **62**(235), 963–975. doi:[10.1017/jog.2016.80](https://doi.org/10.1017/jog.2016.80)

Noël B, Van De Berg WJ, Lhermitte S, Wouters B, Schaffer N and Van Den Broeke MR (2018) Six decades of glacial mass loss in the Canadian Arctic Archipelago. *Journal of Geophysical Research: Earth Surface* **123**(6), 1430–1449. doi:[10.1029/2017jf004304](https://doi.org/10.1029/2017jf004304)

**Pitcher LH and Smith LC** (2019) Supraglacial streams and rivers. *Annual Review of Earth and Planetary Sciences* **47**(1), 421–452. doi:[10.1146/annurev-earth-053018-060212](https://doi.org/10.1146/annurev-earth-053018-060212)

**Rantanen M and 7 others** (2022) The Arctic has warmed nearly four times faster than the globe since 1979. *Communications Earth and Environment* **3**(1). doi:[10.1038/s43247-022-00498-3](https://doi.org/10.1038/s43247-022-00498-3)

**Rawlins LD, Rippin DM, Sole AJ, Livingstone SJ and Yang K** (2023) Seasonal evolution of the supraglacial drainage network at Humboldt Glacier, northern Greenland, between 2016 and 2020. *The Cryosphere* **17**(11), 4729–4750. doi:[10.5194/tc-17-4729-2023](https://doi.org/10.5194/tc-17-4729-2023)

**Rippin DM, Pomfret A and King N** (2015) High resolution mapping of supra-glacial drainage pathways reveals link between micro-channel drainage density, surface roughness and surface reflectance. *Earth Surface Processes and Landforms* **40**(10), 1279–1290. doi:[10.1002/esp.3719](https://doi.org/10.1002/esp.3719)

**Ryser C, Lüthi M, Blindow N, Suckro S, Funk M and Bauder A** (2013) Cold ice in the ablation zone: Its relation to glacier hydrology and ice water content. *Journal of Geophysical Research: Earth Surface* **118**(2), 693–705. doi:[10.1029/2012jf002526](https://doi.org/10.1029/2012jf002526)

**Schoof C** (2010) Ice-sheet acceleration driven by melt supply variability. *Nature* **468**(7325), 803–806. doi:[10.1038/nature09618](https://doi.org/10.1038/nature09618)

**Serreze MC, Raup B, Braun C, Hardy DR and Bradley RS** (2017) Rapid wastage of the Hazen Plateau ice caps, northeastern Ellesmere Island, Nunavut, Canada. *The Cryosphere* **11**(1), 169–177. doi:[10.5194/tc-11-169-2017](https://doi.org/10.5194/tc-11-169-2017)

**Sharp M and 12 others** (2014) Remote sensing of recent glacier changes in the Canadian Arctic. In Kargel JS, Leonard GJ, Bishop MP, Kääb A and Raup BH (eds), *Global Land Ice Measurements from Space*. Springer Berlin / Heidelberg: Praxis-Springer, pp. 205–228. doi:[10.1007/978-3-54079818-7\\_9](https://doi.org/10.1007/978-3-54079818-7_9)

**Smith C and 8 others** (2020) Dickinson Hackweek: Sixty-year record of ice area loss from the marine terminating Sydkap Glacier, southern Ellesmere Island, Nunavut, Canada. *AGU Fall Meeting Abstracts 2020* **2020**, C038–0004.

**St Germain SL and Moorman BJ** (2016) The development of a pulsating supraglacial stream. *Annals of Glaciology* **57**(72), 31–38. doi:[10.1017/aog.2016.16](https://doi.org/10.1017/aog.2016.16)

**St Germain SL and Moorman BJ** (2019) Long-term observations of supraglacial streams on an Arctic glacier. *Journal of Glaciology* **65**(254), 900–911. doi:[10.1017/jog.2019.60](https://doi.org/10.1017/jog.2019.60)

**Thomson LI and Copland L** (2017) Multi-decadal reduction in glacier velocities and mechanisms driving deceleration at polythermal White Glacier, Arctic Canada. *Journal of Glaciology* **63**(239), 450–463. doi:[10.1017/jog.2017.3](https://doi.org/10.1017/jog.2017.3)

**Thomson LI and Copland L** (2018) Changing contribution of peak velocity events to annual velocities following a multi-decadal slowdown at White Glacier. *Annals of Glaciology* **58**(75pt2), 145–154. doi:[10.1017/aog.2017.46](https://doi.org/10.1017/aog.2017.46)

**White A and Copland L** (2018) Area change of glaciers across Northern Ellesmere Island, Nunavut, between ~1999 and ~2015. *Journal of Glaciology* **64**(246), 609–623. doi:[10.1017/jog.2018.49](https://doi.org/10.1017/jog.2018.49)

**Wolken GJ, England JH and Dyke AS** (2008) Changes in late-Neoglacial perennial snow/ice extent and equilibrium-line altitudes in the Queen Elizabeth Islands, Arctic Canada. *The Holocene* **18**(4), 615–627. doi:[10.1177/0959683608089215](https://doi.org/10.1177/0959683608089215)

**Wyatt FR and Sharp MJ** (2015) Linking surface hydrology to flow regimes and patterns of velocity variability on Devon Ice Cap, Nunavut. *Journal of Glaciology* **61**(226), 387–399. doi:[10.3189/2015jog14j109](https://doi.org/10.3189/2015jog14j109)

**Yang K and 8 others** (2018) A new surface meltwater routing model for use on the Greenland Ice Sheet surface. *The Cryosphere* **12**(12), 3791–3811. doi:[10.5194/tc-12-3791-2018](https://doi.org/10.5194/tc-12-3791-2018)

**Yang K and 6 others** (2019) Supraglacial rivers on the northwest Greenland Ice Sheet, Devon Ice Cap, and Barnes Ice Cap mapped using Sentinel-2 imagery. *International Journal of Applied Earth Observation and Geoinformation* **78**, 1–13. doi:[10.1016/j.jag.2019.01.008](https://doi.org/10.1016/j.jag.2019.01.008)

**Yang K, Karlstrom L, Smith LC and Li M** (2017) Automated high-resolution satellite image registration using supraglacial rivers on the Greenland Ice Sheet. *IEEE Journal of Selected Topics in Applied Earth Observations and Remote Sensing* **10**(3), 845–856. doi:[10.1109/jstars.2016.2617822](https://doi.org/10.1109/jstars.2016.2617822)

**Yang K, Li M, Liu Y, Cheng L, Huang Q and Chen Y** (2015a) River detection in remotely sensed imagery using Gabor filtering and path opening. *Remote Sensing* **7**(7), 8779–8802. doi:[10.3390/rs70708779](https://doi.org/10.3390/rs70708779)

**Yang K and Smith LC** (2013) Supraglacial streams on the Greenland Ice Sheet delineated from combined spectral–shape information in high-resolution satellite imagery. *IEEE Geoscience and Remote Sensing Letters* **10**(4), 801–805. doi:[10.1109/lgrs.2012.2224316](https://doi.org/10.1109/lgrs.2012.2224316)

**Zemp M and 58 others** (2025) Community estimate of global glacier mass changes from 2000 to 2023. *Nature* **639**, 382–388. doi:[10.1038/s41586-024-08545-z](https://doi.org/10.1038/s41586-024-08545-z)

## Appendix A: Datasets and example visualization of supraglacial channel mapping.

**Table A1.** Historical aerial photographs used for the qualitative (multidecadal time series) and quantitative (channel delineation) assessments of the supraglacial drainage systems on all five studied glaciers in 1959

Glacier	Roll number	ID	Date	Ground resolution (m)
Sydkap	A16724	0190	13-08-1959	~4
Unnamed 2	A16613	0106	07-07-1959	~0.6
Unnamed 2	A16679	0073	15-07-1959	~0.6
Unnamed 2	A16679	0072	15-07-1959	~4
Unnamed 2	A16726	0084	12-08-1959	~0.6
Unnamed 2	A16794	0023	22-08-1959	~0.6
Unnamed 2	A16974	0025	22-08-1959	~4
John Evans	A16607	0193	05-06-1959	~0.6 and ~4
John Evans	A16607	0192	05-06-1959	~0.6
John Evans	A16616	0059	05-07-1959	~4
Henrietta-Nesmith	A16613	0035	07-07-1959	~0.6
Henrietta-Nesmith	A16679	0155	15-07-1959	~0.6
Henrietta-Nesmith	A16687	0069	28-07-1959	~4
Unnamed 1	A16708	0005	29-07-1959	~0.6

**Table A2.** Satellite imagery used for the qualitative and quantitative time series analyses, including supraglacial channel delineation, sink identification and delineation of the 2020 ELAs

Glacier	Image ID	Platform	Acquisition date	Ground resolution (m)
Sydkap	5 074-138/7 12/08/02 18:28:43 2 J	SPOT-5	02-08-2012	10
Sydkap	S2A_MSIL2A_20160809T190922_N0500_R056_T16XEL_20231001T044540	Sentinel-2	09-08-2016	10
Sydkap	S2A_MSIL2A_20170818T184921_N0500_R113_T16XEL_20230828T114505	Sentinel-2	18-08-2017	10
Sydkap	S2A_MSIL2A_20190814T190921_N0500_R056_T16XEL_20230506T041706	Sentinel-2	14-08-2019	10
Sydkap	S2B_MSIL1C_20200725T183919_N0209_R070_T16XEL_20200725T204817	Sentinel-2	25-07-2020	10
Sydkap	20200810_173013_45_2304	PlanetScope	10-08-2020	3
Sydkap	20200810_174130_88_222b	PlanetScope	10-08-2020	3
Unnamed 2	2 085-141 91-07-05 00:11:45 2 X	SPOT-2	05-07-1991	20
Unnamed 2	AST_L1T_00307192002182828_20150423085645_16236	Terra/ASTER	19-07-2002	15
Unnamed 2	5 083-137 11/07/13 18:59:45 2 J	SPOT-5	13-07-2011	10
Unnamed 2	S2A_MSIL2A_20160813T184922_N0500_R113_T18XVN_20230928T183909	Sentinel-2	13-08-2016	10
Unnamed 2	S2A_MSIL2A_20170817T191911_N0500_R099_T18XVN_20230826T215252	Sentinel-2	17-08-2017	10
Unnamed 2	S2A_MSIL2A_20180802T191911_N0500_R099_T18XVN_20230802T133144	Sentinel-2	02-08-2018	10
Unnamed 2	S2A_MSIL2A_20190814T190921_N0500_R056_T18XVN_20230506T041706	Sentinel-2	14-08-2019	10
Unnamed 2	20200723_000923_09_2257	PlanetScope	23-07-2020	3
Unnamed 2	20200723_000925_31_2257	PlanetScope	23-07-2020	3
Unnamed 2	S2A_MSIL2A_20200806T182921_N0500_R027_T18XWP_20230507T144903	Sentinel-2	06-08-2020	10
Unnamed 2	22AUG02002430-P2AS016259646030_01_P001	WorldView-2	22-08-2022	0.5
Unnamed 2	22AUG02002419-P2AS-016259646030_01_P002	WorldView-2	22-08-2022	0.5
John Evans	1 088-137 87-07-12 19:02:22 2 P	SPOT-1	12-07-1987	20
John Evans	AST_L1T_00307192002182810_20150423085643_1600	Terra/ASTER	19-07-2002	15
John Evans	5 088-137 11/08/03 18:55:19 1 A	SPOT-5	03-08-2011	5
John Evans	S2A_MSIL2A_20160723T191912_N0500_R099_T18XWP_20231007T044659	Sentinel-2	23-07-2016	10
John Evans	S2A_MSIL2A_20170805T183921_N0500_R070_T18XWP_20231001T225130	Sentinel-2	05-08-2017	10
John Evans	S2A_MSIL2A_20180802T191911_N0500_R099_T18XWP_20230802T133144	Sentinel-2	02-08-2018	10
John Evans	S2A_MSIL2A_20190814T190921_N0500_R056_T18XWP_20230506T041706	Sentinel-2	14-08-2019	10
John Evans	20200723_000758_98_105c	PlanetScope	23-07-2020	3
John Evans	20200723_000757_10_105c	PlanetScope	23-07-2020	3
John Evans	S2A_MSIL2A_20200728T193911_N0500_R042_T18XWP_20230324T093756	Sentinel-2	28-07-2020	10
Henrietta-N	1 091-129 87-08-19 20:11:42 1 P Level 1A SAT 0	SPOT-1	19-08-1987	20
Henrietta-N	AST_L1T_00307292000201838_20150410170513_38964	Terra/ASTER	29-07-2000	15
Henrietta-N	AST_L1T_00308282012193314_20150612110915_77182	Terra/ASTER	28-08-2012	15
Henrietta-N	S2A_MSIL2A_20160730T205022_N0500_R057_T18XWS_20231006T211410	Sentinel-2	30-07-2016	10
Henrietta-N	S2A_MSIL2A_20180802T210021_N0500_R100_T18XWS_20230719T190339	Sentinel-2	02-08-2018	10
Henrietta-N	S2A_MSIL2A_20190814T205021_N0500_R057_T18XWS_20230504T233540	Sentinel-2	14-08-2019	10
Henrietta-N	20200724_073642_33_1065	PlanetScope	24-07-2020	3
Henrietta-N	20200724_073643_88_1065	PlanetScope	24-07-2020	3
Henrietta-N	20200724_073645_43_1065	PlanetScope	24-07-2020	3
Henrietta-N	20200724_073646_98_1065	PlanetScope	24-07-2020	3
Henrietta-N	20200724_073648_54_1065	PlanetScope	24-07-2020	3
Henrietta-N	20200724_074509_69_106a	PlanetScope	24-07-2020	3

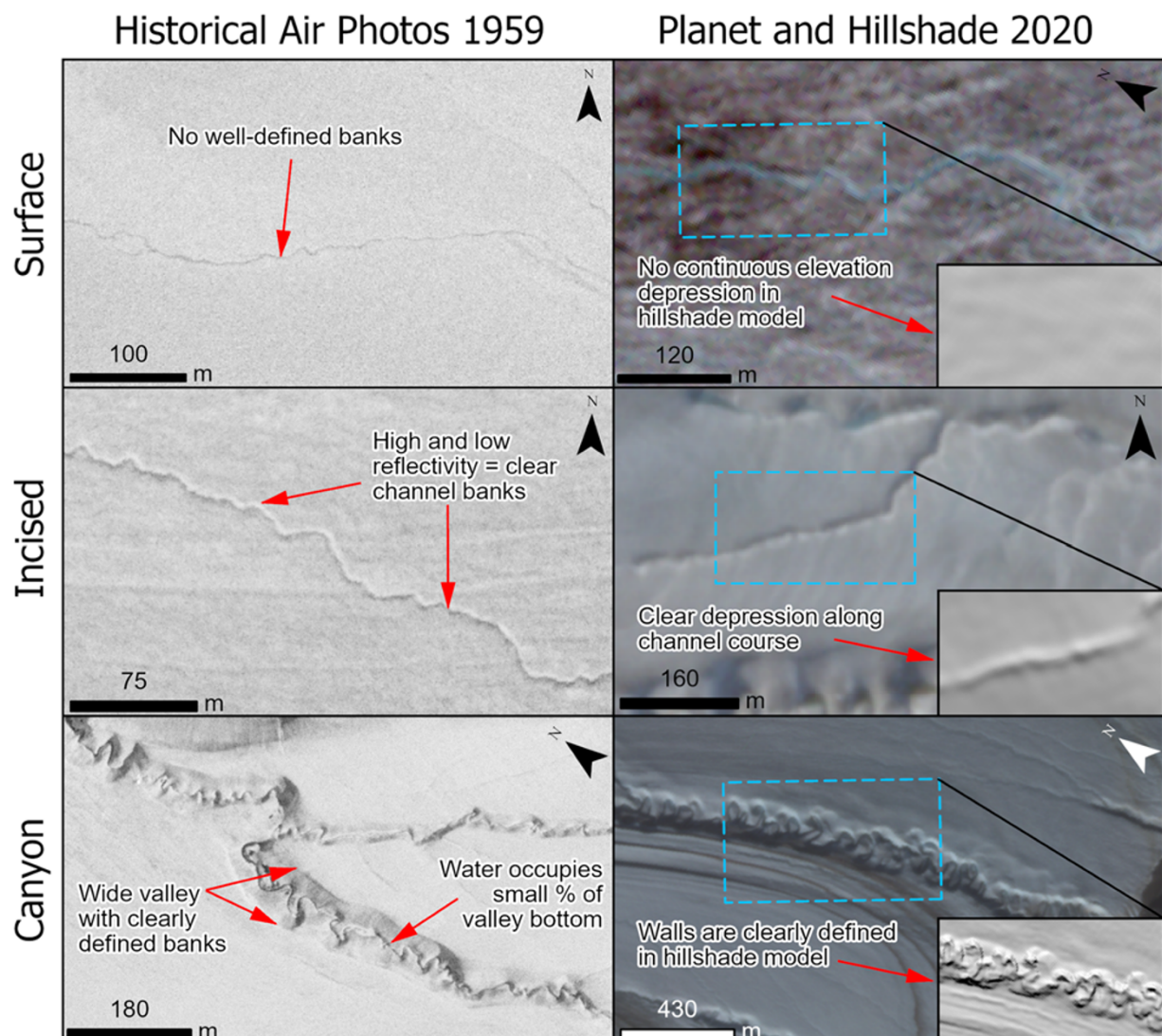
(Continued)

**Table A2.** (Continued.)

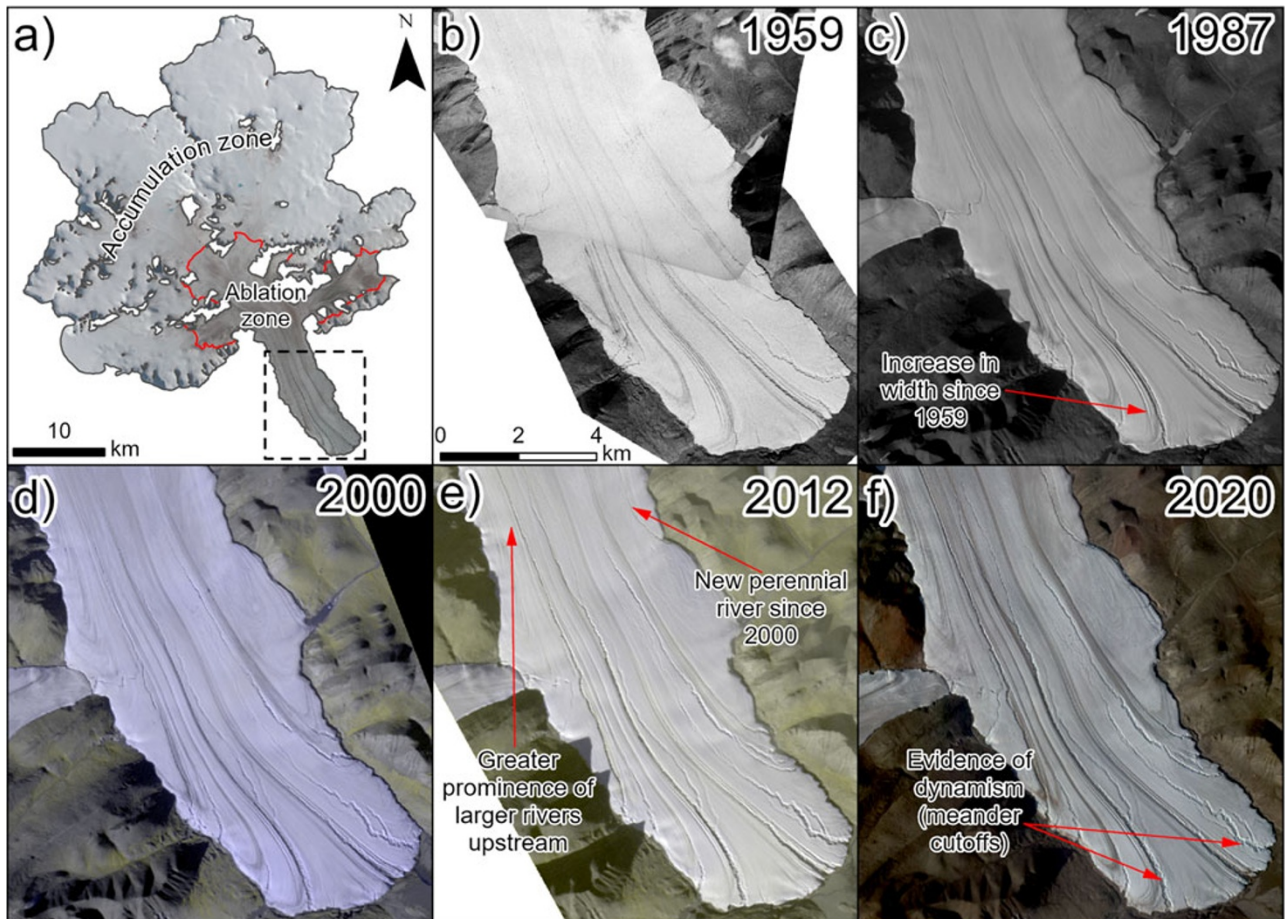
Glacier	Image ID	Platform	Acquisition date	Ground resolution (m)
Henrietta-N	20200724_074511_23_106a	PlanetScope	24-07-2020	3
Henrietta-N	20200724_074512_78_106a	PlanetScope	24-07-2020	3
Henrietta-N	20200724_074514_32_106a	PlanetScope	24-07-2020	3
Henrietta-N	20200724_074515_87_106a	PlanetScope	24-07-2020	3
Henrietta-N	20200724_210831_86_105c	PlanetScope	24-07-2020	3
Henrietta-N	20200724_210833_73_105c	PlanetScope	24-07-2020	3
Henrietta-N	S2A_MSIL2A_20200730T201901_N0500_R071_T18XWS_20230327T110228	Sentinel-2	30-07-2020	10
Henrietta-N	S2A_MSIL2A_20200730T201901_N0500_R071_T19XDL_20230327T110228	Sentinel-2	30-07-2020	10
Unnamed 1	1 091-124 88-08-08 19:44:22 1 X	SPOT-1	08-08-1988	20
Unnamed 1	AST_L1T_00307142009205316_20150528225353_32576	Terra/ASTER	14-07-2009	15
Unnamed 1	20170729_101731_0f2e	PlanetScope	29-07-2017	3
Unnamed 1	20170729_101732_0f2e	PlanetScope	29-07-2017	3
Unnamed 1	20200723_204401_82_2257	PlanetScope	23-07-2020	3
Unnamed 1	20200723_204404_04_2257	PlanetScope	23-07-2020	3
Unnamed 1	20JUL20221803-P2AS-016259646020_01_P001	WorldView-3	20-07-2022	0.5

**Table A3.** ArcticDEM strips used to generate hillshade models and determine the 2020 ELAs for each examined glacier

Glacier	Geocell	Strip ID	Date
Sydkap	n76w086	SETSM_s2s041_WV01_20200502_10200100986EB600_1020010095C00200_2m_lsf_seg1	02-05-2020
Sydkap	n76w087	SETSM_s2s041_WV01_20210425_10200100AF293100_10200100B072F300_2m_lsf_seg1	25-04-2021
Sydkap	n76w086	SETSM_s2s041_WV03_20210514_10400100686F1900_10400100687BC100_2m_lsf_seg1	14-05-2021
Unnamed 2	n78w077	SETSM_s2s041_WV02_20200727_10300100AAB0A800_10300100AB6B5500_2m_lsf_seg1	27-07-2020
Unnamed 2	n78w077	SETSM_s2s041_WV03_20200729_104001005D843300_104001005D875F00_2m_lsf_seg1	29-07-2020
Unnamed 2	n78w077	SETSM_s2s041_WV03_20200729_104001005E8E9600_104001005F2B9D00_2m_lsf_seg1	29-07-2020
John Evans	n79w075	SETSM_s2s041_WV02_20200726_10300100A91BD800_10300100A91F7700_2m_lsf_seg6	26-07-2020
Henrietta-Nesmith	n81w073	SETSM_s2s041_WV02_20200711_10300100A8CCC800_10300100A9BB3E00_2m_lsf_seg1	11-07-2020
Henrietta-Nesmith	n82w073	SETSM_s2s041_WV02_20200711_10300100A91BC200_10300100ABB70600_2m_lsf_seg1	11-07-2020
Henrietta-Nesmith	n82w074	SETSM_s2s041_WV01_20200713_10200100999DFB800_102001009E34D600_2m_lsf_seg1	13-07-2020
Henrietta-Nesmith	n81w075	SETSM_s2s041_WV01_20200714_10200100964C8700_102001009C699B00_2m_lsf_seg1	14-07-2020
Henrietta-Nesmith	n82w075	SETSM_s2s041_WV02_20200715_10300100A7AA3900_10300100AA6E3E00_2m_lsf_seg1	15-07-2020
Henrietta-Nesmith	n81w074	SETSM_s2s041_WV02_20200718_10300100A9F5200_10300100A9A91D00_2m_lsf_seg1	18-07-2020
Henrietta-Nesmith	n81w074	SETSM_s2s041_WV02_20200718_10300100AA7A3E00_10300100AB434300_2m_lsf_seg1	18-07-2020
Unnamed 1	n82w074	SETSM_s2s041_WV03_20200720_104001005D6D5100_104001005F210E00_2m_lsf_seg1	20-07-2020



**Figure A1.** Surface, incised and canyon channels as they appear in the 1959 historical aerial photographs and 2020 PlanetScope imagery, along with a comparison of the same channels in the hillshade model (inset).

**Appendix B: Qualitative time series analysis of glaciers Henrietta-Nesmith and Unnamed 2.**


**Figure B1.** Channel evolution on Henrietta-Nesmith Glacier between 1959 and 2020. (a) Overview of the glacier, with the lower ablation area shown in parts (b–f) outlined by the black box. The red line represents the estimated 2020 ELA at  $1253 \pm 77$  m a.s.l. (b)  $\sim 0.6$  m resolution historical aerial photo, (c) 20 m resolution SPOT-1 image, (d) and (e) 15 m resolution ASTER image, (f) 3 m resolution PlanetScope image. See Tables A1 and A2 for image dates.

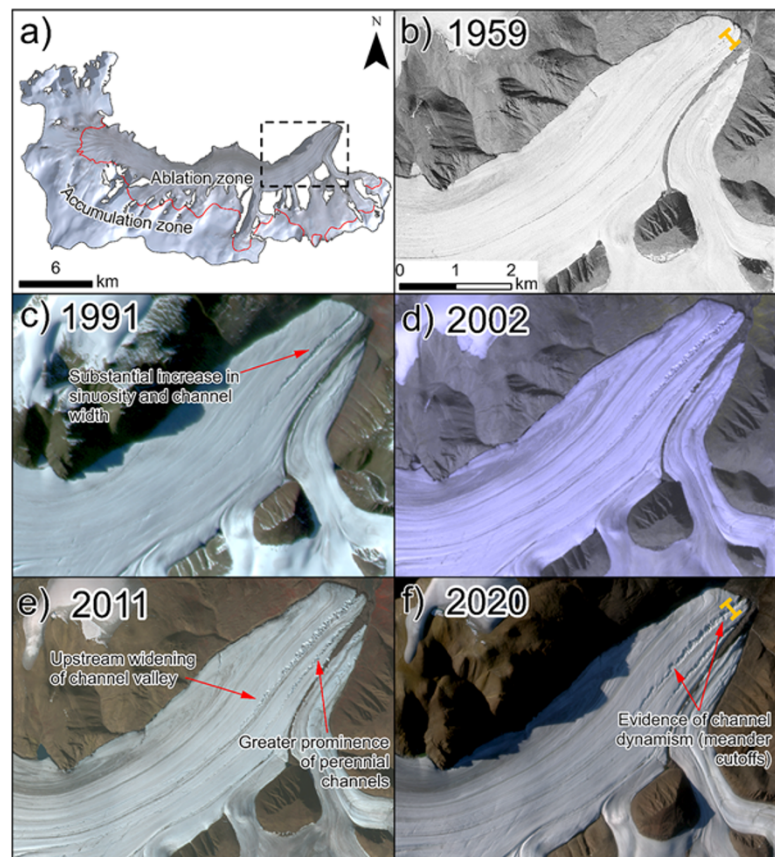


**Figure B2.** Channel evolution on Unnamed 2 Glacier between 1959 and 2020. (a) Overview of the glacier, with the terminus area shown in parts (b–f) outlined by the black box. The red line represents the estimated 2020 ELA at  $1045 \pm 50$  m a.s.l. The orange cross-section line marks the area where channel width was compared over time. (b)  $\sim 0.6$  m resolution historical aerial photo, (c) 20 m resolution SPOT-2 image, (d) 15 m resolution ASTER image, (e) 10 m resolution SPOT-5 image, (f) 3 m resolution PlanetScope image. See Tables A1 and A2 for image dates.

### Appendix C: Trends and significance values for surface mass balance components.

**Table C1.** Rate of change (slope,  $\theta$ ,  $\text{mm a}^{-1}$ ) and significance values ( $p$ ) for gains, losses and net annual specific SMB over the period 1964–2020 across the (a) ablation and (b) accumulation areas of the five studied glaciers, derived from the regional climate model RACMO2.3

Glacier	Gains		Losses		Net annual	
	$\theta$	$p$	$\theta$	$p$	$\theta$	$p$
<b>a) Ablation</b>						
Unnamed 1	2.65	0.01	-6.24	$7.9 \times 10^{-6}$	-3.59	0.034
Henrietta-Nesmith	-0.84	0.0007	-11.47	$7.1 \times 10^{-9}$	-12.32	$5.6 \times 10^{-9}$
John Evans	-0.52	0.5	-9.55	0.0003	-10.07	0.0008
Unnamed 2	-0.04	0.9	-10.67	$3.1 \times 10^{-7}$	-10.71	$2.3 \times 10^{-6}$
Sydkap	-1.94	0.009	-13.00	0.0001	-14.94	$6.8 \times 10^{-5}$
<b>b) Accumulation</b>						
Henrietta-Nesmith	-0.70	0.004	-1.00	$1.3 \times 10^{-6}$	-1.70	$3.5 \times 10^{-6}$
John Evans	-2.05	0.09	-8.59	0.0004	-10.64	0.0009
Unnamed 2	-0.48	0.4	-5.57	$2.3 \times 10^{-6}$	-6.06	$5.5 \times 10^{-5}$
Sydkap	-1.68	0.01	-6.26	$2.0 \times 10^{-5}$	-7.94	$3.7 \times 10^{-5}$

Note: Unnamed 1 was excluded from the accumulation area analysis as its surface area is now completely within the ablation zone.